

Inner crust of neutron stars: Unified description of structure and superconductivity

Dmitry Kobayakov^{1,*} and Xavier Viñas^{2,3,4,†}

¹*Institute of Applied Physics of the Russian Academy of Sciences, 603950 Nizhny Novgorod, Russia*

²*Departament de Física Quàntica i Astrofísica (FQA),*

Universitat de Barcelona (UB), Martí i Franquès 1, E-08028 Barcelona, Spain

³*Institut de Ciències del Cosmos (ICCUB), Universitat de Barcelona (UB), Martí i Franquès 1, E-08028 Barcelona, Spain*

⁴*Institut Menorquí d'Estudis, Camí des Castell 28, 07702 Maó, Spain*

Using the Skyrme model Sk χ 450 constrained by the chiral effective field theory and the ground-state energies of doubly-magic nuclei, we explore the macroscopic static energy spectrum of dense matter. Structure of the matter is idealized as 1-, 2- or 3-dimensional periodic Coulomb lattices (pasta phases) at average baryon density in the range of $0.005n_0 - 0.5n_0$ with $n_0 \sim 0.16 \text{ fm}^{-3}$, corresponding to the inner crust of neutron stars. In the earlier work, the bulk and the surface nuclear properties in this scenario were described on the basis of different nuclear interactions. As a result, predictions for the inner crust structure based on those numerical results are not necessarily self-consistent. In this work, we solve this problem by describing the nuclear properties and proton-proton Cooper pairing in a unified manner, *i.e.* based on the same nuclear interaction. We calculate the surface tension to the leading order (planar surface) and to the next-to-leading order (from nonzero principal curvature) at the Extended Thomas-Fermi level. Next, we develop and solve a system of equations within the compressible liquid drop model (LDM), which provides us with all necessary information about the macroscopic static energy spectrum of the nuclear structure. We find that the curvature corrections change the ground state in a relevant way. We also find that, typically, the energy differences between the different pasta phases are less than the thermal energy for temperatures $\sim 10^8 - 10^9$ K, which implies that the real nuclear pasta phases are likely polymorphic. Finally, for 1-dimensional pasta phase we evaluate the superconducting coherence length of protons, the London penetration depth and the superconducting energy gap. Our results offer a preliminary insight into rich magnetic properties of the pasta phases.

I. INTRODUCTION

The physics of neutron star interiors represents a major challenge for both nuclear physics and astrophysics. There are robust theoretical models for describing the structure of neutron stars up to densities of the order of 1-2 times the saturation baryon number density in symmetric nuclear matter ($n_0 \sim 0.16 \text{ fm}^{-3}$). However, in the central part of the core of neutron stars the matter is expected to be at significantly higher densities. At present, no reliable theoretical model exists to describe matter at such high density. Fortunately, observations of neutron stars suggest physical phenomena that likely probe the global structure of neutron stars including the central part of the core. Among those are the giant magnetar flares and the corresponding quasi-periodic oscillations in the afterglows. As is apparent from the energetic scale of the phenomenon, it involves hydromagnetic waves spreading across the entire star.

Understanding the hydromagnetic waves on a global stellar scale requires to specify properties of the electrical conduction of matter and its interaction with the magnetic field. In this paper, we will study the nature of the electrical conductivity in the inner crust with emphasis on superconductivity of protons and the microscopic structure of the pasta phases.

The pasta phases appear in the bottom part of the inner crust as nonspherical nuclear clusters [1]. Since the proton pairing is generally expected in nuclear matter around the nuclear saturation density [2], the protons inside these nonspherical struc-

tures should be superconducting [3–5]. However, it is now well-known [6] that magnitude of the proton pairing gap is very sensitive to both the baryon density and the proton fraction. Thus, understanding of the essential details of superconductivity in the pasta phases requires a complete microscopic description of the structure of the inner crust of neutron stars.

Information regarding the microscopic structure of the pasta phases is crucial for the correct choice of the superconductivity model, which is theoretically applicable for the pure structures of the pasta phases. For instance, let us consider the 1-dimensional pure pasta structure (*lasagna phase*, or 1N phase), where the slabs of superconducting nuclear matter are separated by regions containing the pure neutron liquid. The distance between the nearest interfaces of two adjacent slabs is denoted by d_L , while the width of the slab is $2r_N$. Under the expected physical conditions, such lasagna phase is similar to a layered superconductor and should be described by different mean-field models depending on the microscopic parameters. When the tunneling of Cooper pairs between the slabs through the insulating pure neutron liquid is small, the appropriate description is given by a discreet (in the sense that the slabs are individual) model of superconductivity, for example, the Lawrence and Doniach model. On the contrary, when the tunneling between the slabs is significant, the system should be described as a continuous (in the sense that the superconducting density is averaged across many slabs) model of superconductivity, for example, the Ginzburg-Landau (GL) model [7–9].

As is well-known [7–9], the significance of the Cooper pair tunneling is quantified by the relative magnitude of the coherence length ξ associated with the uniform matter inside the superconducting slab and the separation distance d_L . A con-

* dmitry.kobayakov@appl.sci-nnov.ru

† xavier@fqa.ub.edu

tinuous model for superconductivity can be used when $\xi \gtrsim d_L$, while at $\xi \lesssim d_L$, the discrete model should be preferred.

The continuous model is generally valid at temperatures close to the superconducting critical temperature (in this case $\xi \rightarrow +\infty$), but may be invalid in the low-temperature regime $T \rightarrow 0$ well below the critical temperature, if $\xi < d_L$. In our system though, the open question at present is whether the superconducting critical temperature is smaller or larger than the lattice melting temperature. In a recent work, Zhang and Pethick [5] have used a continuous model for superconductivity in the lasagna phase and implicitly assumed that the superconducting gap energy is constant across the entire lasagna phase.

We are interested in a quantitative description of the energy landscape for the equilibrium pasta structures taking into account superconductivity of protons. While the magnetic properties of cold neutron stars have long been recognized as an observational clue to the internal stellar structure, however, their understanding has been hindered by the possible presence of superconductivity near the crust-core boundary. Another strong source of complication is the possible presence of the pasta phases, because those phases are anisotropic and multiply connected locally, in contrast to the isotropic locally (apart from the global stellar length scale) singly-connected superconductor in the outer core, which makes their magnetic properties very different from those of the “simple” bulk superconductor in the outer core.

A comprehensive study of the inner crust including the pairing correlations should be performed on the basis of the complete thermodynamic potential (the Gibbs free energy) including such variables as temperature, entropy per particle, the magnetic induction, the given (external) magnetic field and the baryon number density. In this path, we will make the first step and study the internal energy per baryon in the pasta phases. Also we will establish a basis for further studies of superconductivity by studying of the superconducting coherence length and the pairing gap of protons in the pasta phases. Effects of entropy and the magnetic field will be studied in the future work.

Within a mean-field approach, the most sophisticated description of the inner crust is provided by Hartree-Fock (HF) calculations in the Wigner-Seitz (WS) cells, which are complicated owing to the presence of the neutron liquid and the need to deal with non-spherical geometries. There are many Hartree-Fock calculations of spherical nuclei since the seminal paper of Negele and Vautherin [14] (see also [15] and references therein) and also more recently 3-dimensional mean-field calculations using non-relativistic and relativistic energy density functionals and classical and quantum molecular dynamics simulations (see for further details the recent paper by Newton et al. [13] where the state-of-the-art of nuclear pasta calculations is discussed in detail). However, these sophisticated calculations only provide partial information about the structure of the inner crust and to date no systematic calculations to obtain the complete equation of state in the inner crust have been made. Large scale calculations of the inner crust are usually performed with the help of semiclassical approaches based on the Thomas-Fermi (TF) approximation

(see [16] for more details) or through the LDM.

In this paper we will work within compressible liquid drop model (LDM), which is a powerful tool offering a simple physical interpretation of complicated many-body nucleon effects. This model is based on a convenient choice of the collective degrees of freedom. It has been used in the pioneering study of the nuclei surrounded by dripped neutrons [17] and has been crucial in the theoretical prediction of the nonspherical nuclei in the inner crust of neutron stars [18, 19].

Within the LDM, the properties of the nuclear surface, as for instance the surface tension and the behavior of the neutron and proton density profiles, play an essential role. The surface tension has been always represented in approximate manner, based, for example, on the leptodermous expansion of the binding energy of nuclear systems [20, 21]. The orders of approximation correspond to the power of the moment in the integrand in Eqs. (D1), (D3) and (D5). The leading approximation is to calculate the surface tension associated with the planar surface (when the principal curvature is zero) with a sharp density profile of protons and use it for description of the nuclear clusters. The approximate character of the surface tension in this case comes from the fact that in reality, the principal curvature of the surface of nuclear cluster is nonzero, the proton surface is smeared, and there is a film of adsorbed neutrons at the surface of nuclear cluster. In the next-to-leading approximation, the energy contribution due to a nonzero principal curvature is included, while the proton surface is kept sharp and no neutrons adsorbed; this approximation is elaborated in this paper. In the next orders of approximation, which are left for the future work, the smearing of the proton surface and neutrons adsorbed on the nucleus surface are included.

The next-to-leading approximation was considered in many recent LDM calculations [22–29]. Importantly, in those calculations the surface and curvature contributions to the energy density functional were taken from parameterizations originally proposed by Lattimer, Pethick, Ravenhall and Lamb [30, 31] generalized later on by Lorentz and Pethick [32]. Here, we improve on the earlier calculations and extract the planar and curvature contributions to the surface tension from a self-consistent extended Thomas-Fermi (ETF) [33] calculation performed using the same interaction that describes the bulk part in the LDM, following closely the method described in detail in Refs. [34, 35], which is summarized in Appendix D.

The potential energy contribution to the energy density functional provided by Skyrme forces can be expressed in terms of the nucleon densities in uniform nuclear matter n_n and n_p , and the square of their gradients, $(\nabla n_n)^2$ and $(\nabla n_p)^2$. In the ETF approach, the kinetic energy is also an energy density functional that is expanded in powers of \hbar^2 . In this work we take only the two first terms of this expansion. The leading order term correspond to the bulk, which is expressed through the TF kinetic energy densities for neutrons and protons. The next-to-leading order term includes second order gradients of the nuclear densities and effective masses as well as a contribution of the semiclassical spin density, as it can be seen in Eqs. (A1), (A2) and (A3).

The paper is organized as follows. Section II presents ba-

sic equations of the LDM of nuclear matter, which are explained in detail in Appendices B and C. Appendix A lists the details of the nuclear interaction energy functional used in the paper and a discussion of the nuclear matter properties. Appendix D describes our self-consistent numerical results based on a single equation of state for both the nuclear bulk and the surface properties. Section III is reserved for the numerical results on solution of the LDM equations, evaluation of thermal effects, the workfunction to transfer proton from nucleus to the pure neutron matter, the coherence length of superconducting protons and the magnitude of the pairing energy gap. In Section IV we analyze the superconductivity in the 1-dimensional pasta phase by studying the coherence length of superconducting protons and the stress tensor in the superconducting-superfluid mixture relevant to the outer core and the inner crust of neutron stars. Section V summarizes the paper.

II. LIQUID DROP MODEL

A. Basic approximations

We assume that the matter in the inner crust of neutron stars is in a low-energy static state and the nuclei form a Coulomb crystal with a uniform electron background. Therefore, it is a reasonable approximation to represent the real matter as a model with ideal lattice and nuclei with sharp edges. Inside these nuclei, the matter is assumed to have a uniform density of baryons n with a local number density of protons $n_p = xn$, x being the proton fraction, and the local density of neutrons $n_{ni} = (1-x)n$. The voids between the nuclei are filled by the dripped neutrons with a uniform density n_{no} .

We shall work in the spherical Wigner-Seitz (WS) cell approximation and focus on a single unit cell with volume V_c and the total number of neutrons N_n and protons N_p :

$$n_b = \frac{N_p + N_n}{V_c}. \quad (1)$$

A cell either contains a nucleus surrounded by the neutron liquid (1N, 2N, 3N), or it is entirely filled by the nuclear matter except in its center, where there is a bubble filled with a pure neutron liquid (1B, 2B, 3B). The nuclear matter and the pure neutron liquid are separated by a spherical interface in case of 3N and 3B, by a cylindrical interface in case of 2N and 2B, and by a planar interface in case of 1N. The WS cells have a finite lattice period along three spatial dimensions (for 3N and 3B configurations), or along two dimensions (for 2N and 2B configurations), or along only a single dimension (for 1N configuration). The length or the area of the cell along the direction with a continuous translational symmetry is equal to the unit of length or the unit of area, respectively.

Notice that in the one-dimensional symmetry, the description in terms of 1N is equivalent to the description in terms of the 1B with an appropriate change in variables, and thus, the results for 1N and 1B can be combined and represented as a single case, which is denoted briefly as 1N. Still, it is important that the volume fraction for 1N corresponds to the ratio

between the volume of nucleus and the unit cell, while the volume fraction for 1B corresponds to the ratio between the volume of neutron-filled bubble and the unit cell, hence the variable u used for the volume fraction in the phase of nuclear clusters is distinct from the variable u^{bub} used for the volume fraction in the phase of nuclear bubbles. To keep the theory as clear as possible, in Appendix we present the formulas for nuclei and for bubbles separately.

B. Basic equations

As it is explained in Appendix B, within a WS cell the total energy density, Eq. (B19), for (1N, 2N, 3N) phases can be written as a sum of the following pieces:

$$w_{\text{tot}} = w_{\text{nuc}} + w_{\text{p,surf}} + w_{\text{C+L}} + w_{\text{no}} + w_e + w_{\text{curv}} + w_{\text{sk}} + w_{\text{dc}}, \quad (2)$$

where w_{nuc} is the bulk (uniform) energy density of the nuclear cluster. The terms $w_{\text{p,surf}}$ and w_{curv} are the nuclear surface contributions, where the former describes the *planar surface* contribution and the latter describes the curvature of the interface. The contribution from the dripped neutron liquid is given by w_{no} and the kinetic energy of the electron background by w_e . The Coulomb energy term $w_{\text{C+L}}$, collects the self-energy of protons in the nuclear cluster and of electrons distributed in the WS cell as well as the proton-electron lattice energy. Finally, the terms w_{sk} (the contribution from the neutron skin in the planar interface) and w_{dc} (its correction due to curvature of the interface) provide the energy contribution due to the adsorbed neutrons at the surface of the cluster. Analogously, the energy density for bubble phases is described by Eq. (C19).

The basic equations are a set of coupled algebraic equations, which can be obtained from the variational procedure as specified in Appendices B and C. That the variational equations are satisfied implies the system state is in the local energy minimum. In this paper, we will find the solution with $n_{\text{sk}} = n_{\text{dc}} = 0$, which implies neglect the neutron skin energy density correction and also neglect of the width of the thin layer where the neutron number density smoothly transitions between its values inside and outside of the nucleus.

With the mean baryon density n_b given as an external parameter, the four unknowns are the proton fraction inside the nucleus, the nucleus (or the bubble) radius, the baryon number density inside the nuclear matter phase and the neutron number density inside the pure neutron liquid:

$$\{x, r_N \text{ (or } r_B), n, n_{no}\}. \quad (3)$$

The full set of basic (variational) equations contains four algebraic equations:

$$\mu_e = \mu_{ni} - \mu_{pi}, \quad (4)$$

$$w_{\text{p,surf}} + 2w_{\text{curv}} = 2w_{\text{C+L}}, \quad (5)$$

$$\mu_{ni} = \mu_{no}, \quad (6)$$

$$P_i = P_o. \quad (7)$$

The explicit derivation of Eqs. (4)-(7) is detailed in Appendices B and C. The quantities in Eqs. (4)-(7) are defined for nuclei in Eqs. (B42), (B49) and (B53); (B32), (B21), (B22) and (B27); (B48), (B49) and (B50); (B60), (B61) and (B62); for bubbles in Eqs. (C40), (C47) and (C49); (C30), (C21), (C22) and (C25); (C46), (C47) and (C48); (C56), (C57) and (C58). Notice that our definitions of the pressure inside the nucleus P_i and of the chemical potential of neutrons inside the nucleus μ_{ni} , include both the bulk and the surface contributions, which differs from the notation used by Lim and Holt [22].

In order to solve Eqs. (4)-(7), as a first step we choose the ranges of values of n and n_{no} and represent them as uniform arrays of points. For each pair of values of n and n_{no} from the chosen ranges we find from Eq. (4) the ‘‘equilibrium’’ value of $x = x(n, n_{no})$. In this step we express the volume fraction u from Eqs. (B17) and (C17) as

$$u = \frac{n_b - n_{no}}{n - n_{no}}, \quad u^{\text{bub}} = \frac{n - n_b}{n - n_{no}}, \quad (8)$$

which allows to find r_N and r_B using Eq. (5).

In the next step we find the pairs of variables (n, n_{no}) that satisfy the rest two of the variational equations, Eqs. (6) and (7). As a result, we obtain two curves on the plane (n, n_{no}) , which might intersect thereby determining the point of the equilibrium. Having determined the intersection point, we have found all the independent variables of the problem and thus, the solution is accomplished. The calculations including the neutron skin corrections will be presented elsewhere.

III. NUMERICAL RESULTS

A. Comparison with earlier work

1. Surface tension in LDM

We start with a numerical verification of our algorithm and reproduce the earlier landmark results, in particular, the appearance of various pasta phases and their transition densities as given in Table III of [22].

As is described in the Appendix D, we have computed self-consistently the surface tension $\sigma_s(x)$ and the curvature correction $\sigma_c(x)$ using the same nuclear interaction, Sk χ 450, as for calculating the bulk. To obtain the main result of this paper, we use directly the numerical data given in Table III for $\sigma_s(x)$, $\sigma_c(x)$ and their derivatives.

This is in contrast with earlier LDM calculations, where different equations of state were used for describing the bulk matter but with a surface tension given by an analytical expression depending on few parameters [30–32]. For instance, Eq. (9) of [22] suggests the following fit

$$\sigma_s^{\text{fit}}(x) = \sigma_0 \frac{2^{\alpha+1} + q}{(1-x)^{-\alpha} + q + x^{-\alpha}}, \quad (9)$$

where the numerical values of the parameters are:

$$\sigma_0 = 1.186, \quad \alpha = 3.4, \quad q = 46.748. \quad (10)$$

	η (Case 1)	η (Case 2)	η (Case 3)
3N-2N	0.4061	0.4025 \pm 0.002	0.3068 \pm 0.002
2N-1N	0.4715	0.4664 \pm 0.002	0.3666 \pm 0.002
1N-2B	0.5361	0.5342 \pm 0.002	–
2B-3B	0.5502	0.5501 \pm 0.002	–
3B-Uni.	0.5624	0.5621 \pm 0.002	–
1N-Uni.	–	–	0.5581 \pm 0.002
η_{uni}^*	–	0.5508	0.5508
η_{p}^*	–	0.5770 \pm 0.002	0.5771 \pm 0.002

TABLE I. The baryon number densities $\eta \equiv n_b/n_0$ at which the solution with the minimum energy per baryon changes its symmetry type (between 1N, 2N, 3N, 2B, 3B phases), or η_{uni}^* at which the uniform nuclear matter is unstable with respect to modulations of the nucleon densities, or η_{p}^* at which the proton drip occurs, in various cases. Case 1: Output data from Table III of [22]. Case 2: Solutions to Eqs. (4)-(7) with $\sigma_c = 0$ and with σ_s from Eqs. (9) and (10). Case 3: Solutions to Eqs. (4)-(7) with σ_s and σ_c from Table III. The quantity η_{uni}^* is found from [22] (see Eq. (30) and Table V in [22]). The quantity η_{p}^* is found from our solution for the workfunction $\Delta\mu_p$ shown in Fig. 5.

We have found that our numerical data on $\sigma_s(x)$ given in Table III can also be fitted by the function Eq. (9) with the following coefficients:

$$\sigma_0 = 1.1110, \quad \alpha = 3.5281, \quad q = 39.3491. \quad (11)$$

In order to check our numerical algorithm, we compute the inner crust structure using Eq. (9) with the parameters given in Eq. (10) and discarding the curvature contribution. We calculate the transition densities between different structures with numerical error bars and display the results in the third column of Table I (marked as Case 2). A good agreement with the earlier results due to Lim and Holt [22] is observed, thereby providing an independent verification of our numerical algorithm. We have also verified that the both parameterizations, Eqs. (11) and (10) with $\sigma_c = 0$ in both cases, lead to two different solutions of the variational equations with the difference being a small quantity.

As a next step, we include both the planar surface contribution $\sigma_s(x)$ and the curvature contribution $\sigma_c(x)$, using the numerical data given in Table III for $\sigma_s(x)$, $\sigma_c(x)$ and their derivatives. The transitions between different configurations are listed in the fourth column of Table I (marked as Case 3). A comparison between the results shown in the the second and fourth columns of Table I (marked as Case 1 and Case 3) suggests that, the inclusion of $\sigma_c(x)$ in this paper provides a qualitative difference for the ground state of the inner crust matter, as compared with the ground state predicted earlier in [22].

2. Towards a realistic structure of the inner crust

The idea that the inner crust might be polycrystalline has been discussed in Refs. [10, 11]. Lately, Zhang and Pethick

[12] have considered a model of disorder in the pasta phase at a given baryon density (in the absence of the magnetic field), corresponding to a collection of monocrystals of large size with the structure oriented at different angles relative to each other. Still, another option is that the structure orientation varies smoothly in space, similarly as occurs in laboratory liquid crystals [11]. Later, Newton *et al.* [13] have suggested that at a constant pressure (in the absence of the magnetic field), several pasta structures are frozen into domains with size of the order of 1-50 times the lattice spacing and over which the local density and electron fraction can vary. The numerical results of Newton *et al.* [13] on the basis of a thermodynamic potential $E + PV$ ignoring the magnetic field and entropy, where E is the internal energy per particle, P is pressure and V is specific volume, have suggested that the structure of pasta phases might be amorphous, *i.e.* without a long-range order.

It seems that a further exploration of thermodynamic properties of the pasta phases on the basis of the complete Gibbs free energy, that includes the entropy and the magnetic induction, is necessary in order to establish definitively, which of the solid phases – *amorphous*, *crystalline* or *polycrystalline*, *polymorphous* or *pure* (thermodynamic) – are expected as a result of cooling process in a real neutron star. Notably, the additional complication is that the result of cooling in a real system is affected by many factors including: The order in which the system experiences the liquid-solid phase transition (the formation of cold solid structure from a warm liquid plasma in the inner crust) and the superfluid-superconducting phase transitions, the cooling rate as compared to rate of relaxation of polymorphic crystals to the thermodynamical phase (characterized by the global minimum of the Gibbs free energy), local fluctuations of the proton fraction, structural defects of the solid-state plasma configurations, mechanical vibrations and the local magnetic field.

B. Basic solution with corrections for curvature of thin nuclear surface

In this calculation we have incorporated the curvature correction to the surface tension, which is a contribution to the energy due to the principal curvature of a thin nuclear surface without finite-width corrections. Here, in order to use our self-consistent numerical results (as given in Table III) on the leading (planar surface) contribution $\sigma_s(x)$ and the next-to-leading (curvature) correction $\sigma_c(x)$, for the surface tension of a thin surface, we represent these functions numerically with the help of spline interpolation – in this way we avoid choosing any fitting parameters such as in Eq. (9). By following the scheme of solution of the variational equations explained above we find the four basic variables, $\{n, x, r_N \text{ or } r_B, n_{no}\}$ as functions of mean (averaged across the WS cell) baryon density n_b scaled by the saturation density in symmetric nuclear matter n_0 and display them in Figs. 1–4.

Figures 1–4 show, correspondingly, as functions of n_b : The proton fraction x inside the nucleus (or outside the bubble) in Fig. 1, the nucleus radius r_N (or the scaled bubble radius,

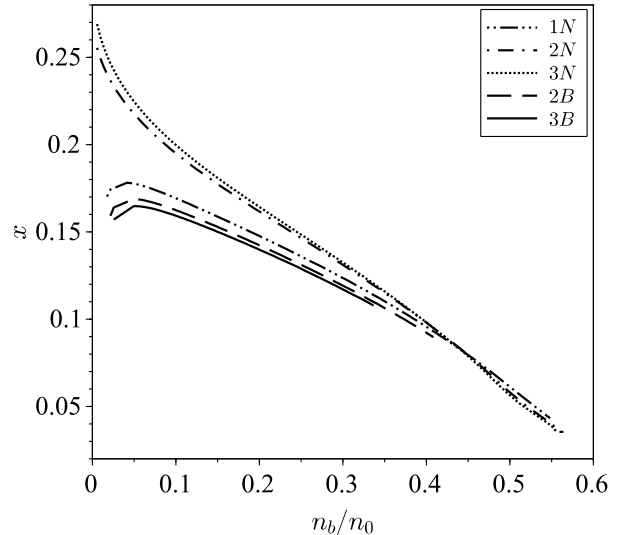


FIG. 1. Solution to the basic equations of equilibrium, Eqs. (4)-(7): The proton fraction x inside the nucleus, Eq. (B9), and outside the bubble, Eq. (C9), as function of the mean baryon density n_b (scaled by n_0).

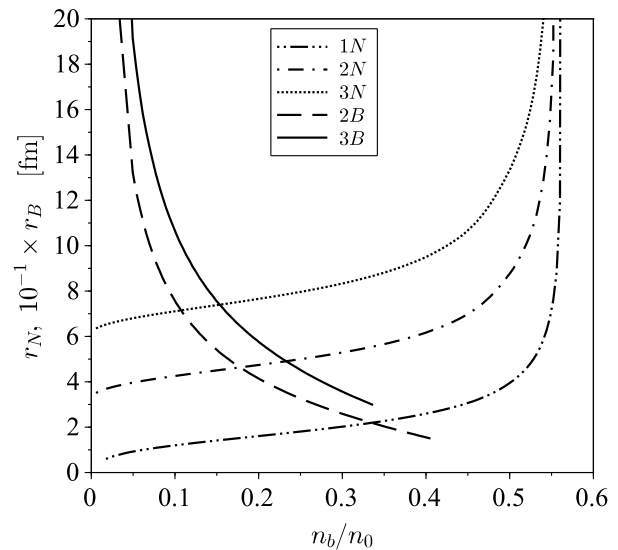


FIG. 2. Solution to the basic equations of equilibrium, Eqs. (4)-(7): The nucleus radius r_N and the scaled bubble radius $r_B/10$ as function of the mean baryon density n_b .

$r_B \times 10^{-1}$) in Fig. 2, the local baryon density n inside the nucleus (or outside the bubble) in Fig. 3, the local number density n_{no} of neutrons outside of the nuclear cluster (or inside the bubble) in Fig. 4.

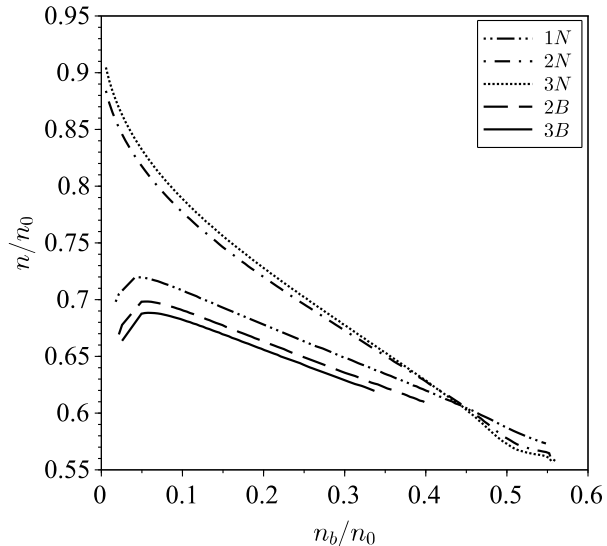


FIG. 3. Solution to the basic equations of equilibrium Eqs. (4)-(7): The baryon number density inside the nucleus and outside the bubble as function of the mean baryon density n_b .

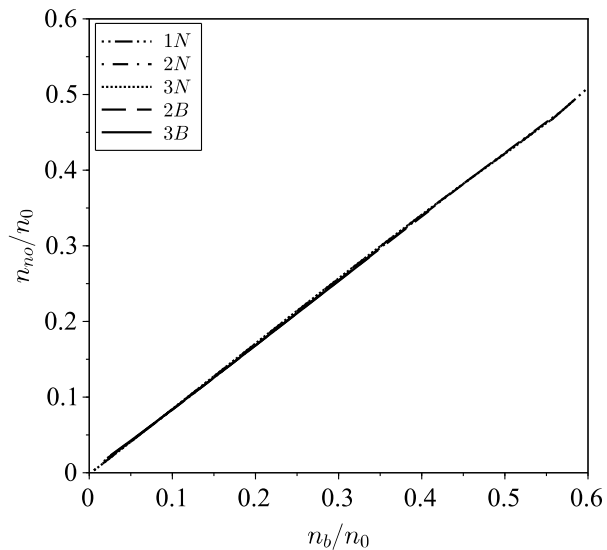


FIG. 4. Solution to the basic equations of equilibrium Eqs. (4)-(7): The baryon number density n_{no} of pure neutron matter outside the nucleus and inside the bubble as function of the mean baryon density n_b .

C. Analysis of the solution

The variables shown in Figs. 1–4 represent a complete and unique solution to the basic equations, however, the appearance of pasta structures is not explicit. As a first step, we compute the difference between the proton chemical potential

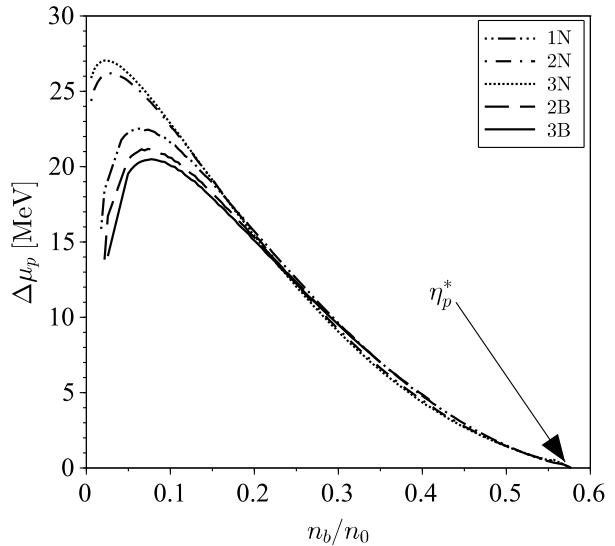


FIG. 5. The workfunction to transfer a proton from the nucleus to the surrounding pure neutron matter, Eq. (12), as function of the mean baryon density n_b , calculated from the results shown in Figs. 1-4. The arrow marks the mean baryon density $\eta_p^* n_0$ corresponding to the proton drip.

inside and outside of the nuclear cluster (Eqs. (B53), (C49) and (B54)),

$$\Delta\mu_p = \mu_{po} - \mu_{pi}, \quad (12)$$

which represents a potential energy barrier created by neutrons that prevents protons flowing from one nuclear cluster to a neighboring one directly through the pure neutron matter between the clusters.

Figure 5 shows $\Delta\mu_p$ as function of the mean baryon density n_b , for five possible pasta phases in the inner crust. From Fig. 5, we observe that at low n_b , the barrier is strong enough to ensure a complete insulation of the pure neutron matter from the proton currents; this fact was also noticed by Zhang and Pethick in [5] who assumed $\Delta\mu_p \sim 6$ MeV. We find, however, that at densities n_b higher than $\sim 0.4n_0$ the barrier smoothly becomes less than 5 MeV, indicating that in some regions of pasta phases, the proton tunneling smoothly becomes important and in this case the pure neutron liquid does not provide efficient insulation against the tunneling proton supercurrents.

Ultimately, at $n_b/n_0 = \eta_p^* \sim 0.58$ the barrier vanishes, which implies that for $n_b/n_0 \geq \eta_p^*$ the protons can freely leave the nucleus and enter the pure neutron liquid. Our LDM calculations using the Sk χ 450 interaction predict that the proton drip occurs at a mean baryon density larger than the critical density η_{uni}^* , for which the uniform nuclear matter corresponds to the ground state. For this interaction, the value of the critical density is $n_b/n_0 = \eta_{uni}^* = 0.5508$, which is computed using Eq. (30) and Table V of [22] and reported in Table I of the present work. This prediction of our model,

$$\eta_{uni}^* < \eta_p^*, \quad (13)$$

have been obtained assuming that the second phase is the pure neutron liquid. With this assumption, the surface energy is a function of the proton fraction only inside the nucleus (see Eqs. (B21) and (B21)). However, in the situation, not considered in this work, when the second phase is a dilute nuclear matter [34–37], the present LDM should be extended in order to take into account nonzero proton fractions both inside and outside the nucleus.

Inserting the solutions shown in Figs. 1–4 into the expressions for the energy density, Eqs. (B18) and (C18), we calculate the total energy density for each of the five structures considered in the crust. Next, we determine the ground-state configuration (with the lowest energy per baryon). Notice that for fixed n_b , the picture in terms of the energy per baryon is equivalent, up to a constant scaling factor, to the picture in terms of the energy density. As a next step, we find all the possible structures whose energy per baryon differs from the minimum energy per baryon by less than the thermal energy $k_B T$.

These results are displayed in Fig. 6, where the minimum energy is shown by black solid line, while the dot markers show the solutions with energy per baryon larger than the minimum energy per baryon by less than the thermal energy $k_B T$, for three different temperatures. The vertical blue lines show the critical densities η_p^* and η_{uni}^* . The calculations for $n_b/n_0 > 0.6$ have been done on a sparser array of values since the uniform matter is the only possible solution in this case.

Figure 6 suggests that even at $T \sim 10^8$ K, the state of a real matter is likely a polymorphic structure, in which locally, nuclear clusters with various types of symmetry (either of 1N, 2N, 3N, 2B, 3B or uniform) coexist. For instance, for n_b below $\sim 0.16n_0$, the system energetically favors only 3N phase. However, for n_b above $\sim 0.16n_0$ and below $\sim 0.297n_0$, the system favors both 3N and 2N phases. For n_b above $\sim 0.297n_0$ and below $\sim 0.345n_0$, or above $\sim 0.41n_0$ and below $\sim 0.515n_0$, the system favors 3N, 2N and 1N phases. Interestingly, for n_b above $\sim 0.515n_0$, the system favors 3N, 2N, 1N and the uniform phases.

IV. SUPERCONDUCTIVITY IN 1-DIMENSIONAL PASTA PHASE AND ASTROPHYSICAL IMPLICATIONS

A. Characteristic physical lengths of protons

Let us focus on the 1N phase of the pasta phases. When the 1N phase is superconducting, its ordered state possess the most exotic magnetic properties among other pasta phases due to its extreme anisotropy.

Figure 6 shows that 1N phase is the ground state in a significant portion of the inner crust [?]. As has been pointed out earlier [3], in 1N phase, the magnetic field effects are especially pronounced when protons are superconducting. In the weak pairing Bardeen-Cooper-Schrieffer approximation, the coherence length, which can be understood as the spatial size of the Cooper pair, reads

$$\xi(0) = \frac{\hbar v_{Fp}}{2\gamma\Delta_p}, \quad (14)$$

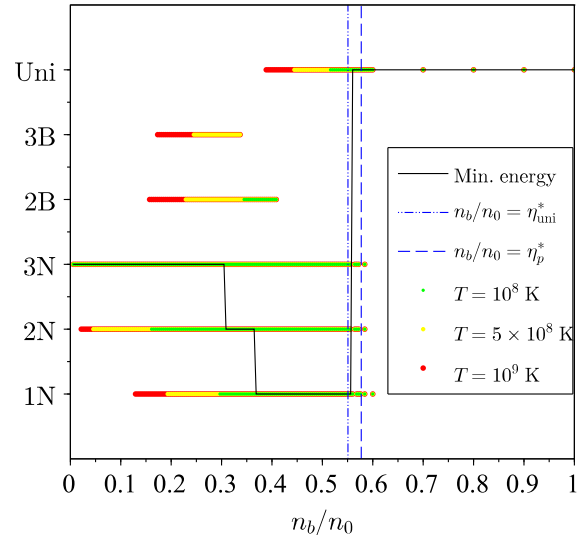


FIG. 6. (Color online) Thermodynamically allowed pasta configurations at three different temperatures T taking the values 10^9 K (red), 5×10^8 K (gold) or 10^8 K (green). Black solid line shows the thermodynamic (the ground-state) configuration characterized by the minimum energy per baryon. The transitions between various pasta phases are seen as jumps of the black solid line, where the almost vertical pieces represent the absence of the data due to the numerical approximations made. The color markers indicate the excited configurations, which satisfy Eqs. (4)–(7), while their energy per baryon is larger than that in the thermodynamic configuration by less than $k_B T$. The dash-dotted lines marks the critical value of n_b at which uniform nuclear matter becomes unstable with respect to long wavelength hydrodynamic fluctuations (see Eq. (A7) for details). The dashed line marks the critical value of n_b at which protons start dripping out from the nuclei (see Fig. 5 for details).

where (0) implies that we neglect the thermal exponential suppression of ξ by virtue of the condition

$$\Delta_p > k_B T \sim 0.01 \text{ MeV}. \quad (15)$$

In Eq. (14), the proton Fermi velocity is $v_{Fp} = \hbar k_p / m_p$, the Euler constant is $\ln \gamma = 0.577$ and $\Delta_p = \Delta_p(n, x)$ is the superconducting energy gap. The proton Fermi wavenumber is given by

$$k_{Fp} = (3\pi^2 Y_p n_b)^{1/3}, \quad (16)$$

where the quantity Y_p (the proton fraction averaged over the WS cell) utilized in [6] is given in variables of the present paper as

$$Y_p = unx/n_b. \quad (17)$$

Calculation of the coherence length ξ of protons requires knowledge of a few elements. The parameters of matter inside the slab with nuclear matter, such as the baryon number density, the proton concentration, are calculated in this paper. Another necessary input is the superconducting energy gap of

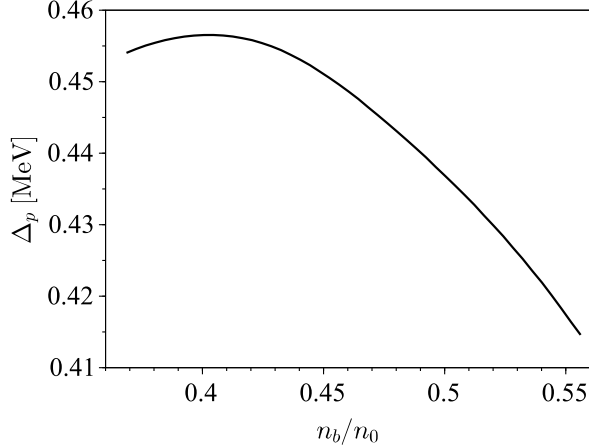


FIG. 7. The superconducting energy gap Δ_p adopted from Fig. 7 of [6], where the k_{Fp} -dependence has been converted into the n_b -dependence with the help of the functions shown in Figs. 1–4 and Eq. (16).

protons. We will use the results from [6], where the energy gap has been obtained from the pairing calculations with the same nuclear interaction Sk χ 450, as has been used to compute the bulk and the surface contributions.

A thermodynamic condition for the existence of the coherent (Cooper) pairing is given by Eq. (15). In order to reveal what part of the 1N phase is expected to be superconducting, we plot in Fig. 7 the superconducting gap energy as function of the mean baryon density across the entire density range of 1N phase. Figure 7 shows that at typical $k_B T \sim 0.01$ MeV, the thermodynamic condition given in Eq. (15) does hold in the entire 1N phase and therefore this phase is expected to host superconducting protons.

The basic magnetic properties of superconducting matter in the 1N phase can be characterized by the ratio d_L/ξ between the interlayer spacing d_L , where

$$d_L = 2(r_c - r_N) = 2(u^{-1} - 1)r_N, \quad (1D \text{ nuclei}) \quad (18)$$

and the coherence length of protons ξ , Eq. (14), and by the Ginzburg-Landau (GL) parameter λ/ξ , where

$$\lambda^2(0) = \frac{m_p c^2}{4\pi e^2 n_p(0)} \quad (19)$$

defines the square of the London penetration depth of the magnetic field for the bulk matter. By using in Eq. (19) the value of the superconducting proton density averaged over the WS cell, we obtain the lower bound on the magnetic penetration depth. If neutrons are introduced between the slabs (such as in the realistic configuration of the 1N phase), the magnetic penetration depth might increase because in this case the superconductor becomes intrinsically multiply-connected as show panels (a) and (b) in Fig. 8.

The magnetic flux through the 1N phase is nonquantized in the case shown in Fig. 8 (a) and is quantized in Fig. 8 (b).

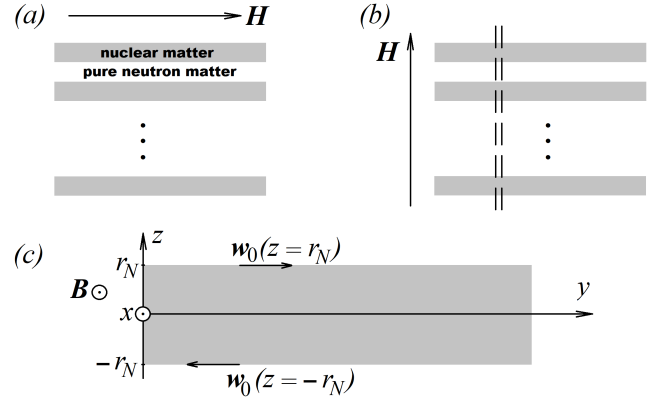


FIG. 8. Schematic representation of a unit length of the ideally ordered 1N phase, which currently is not excluded as a real state of the inner crust at the relevant density range of the inner crust of neutron stars. The three dots in panels (a) and (b) represent the ideal lattice of slabs. Panel (a) shows a configuration with the magnetic field parallel to the slabs. Panel (b) displays a configuration with the magnetic field parallel to the slabs with dashed lines representing the normal core of the magnetic flux tube in the proton superconductor. Panel (c) depicts a single slab within the magnetic induction with arrows representing the neutron-proton momentum lag vector at equilibrium.

Notice that the anisotropy of the 1N phase induces a direction-dependence of the London penetration depth, in contrast to the isotropic Eq. (19). As has been pointed out in [3], for ideally ordered 1N phase without tunneling of Cooper pairs between adjacent superconducting slabs in a parallel magnetic field as shown in Fig. 8 (a), the magnetic penetration depth is macroscopically large.

The GL parameter λ/ξ indicates whether the superconductor is type-I or type-II [39]. The numerical results reported in this paper allow to evaluate the GL parameter along with other characteristic quantities of the proton superconductor in the 1-dimensional pasta phase.

Figure 9 shows the dependence of the parameters d_L , r_N and ξ in the 1N phase on the mean baryon density n_b , where we also plot the scaled London penetration depth λ , the characteristic screening length k_{TFe}^{-1} in the electron background and the inverse Fermi wavenumber of the electrons k_e^{-1} . Here,

$$k_{TFe}^2 = 4\pi e^2 \frac{\partial n_e}{\partial \mu_e}. \quad (20)$$

with n_e and μ_e given by Eqs. (B26) and (B41), correspondingly, so $\partial n_e / \partial \mu_e = k_e^2 / \pi^2 \hbar c$, where

$$k_e^3 = 3\pi^2 n_e. \quad (21)$$

In Fig. 9, we observe that $\lambda/\xi > \sqrt{2}$ in the entire range of n_b corresponding to 1N phase and therefore the 1N phase is expected to be in the type-II regime of superconductivity.

Physically, ξ provides an estimate for the size of the normal core of the quantum magnetic flux tube. In the normal core,

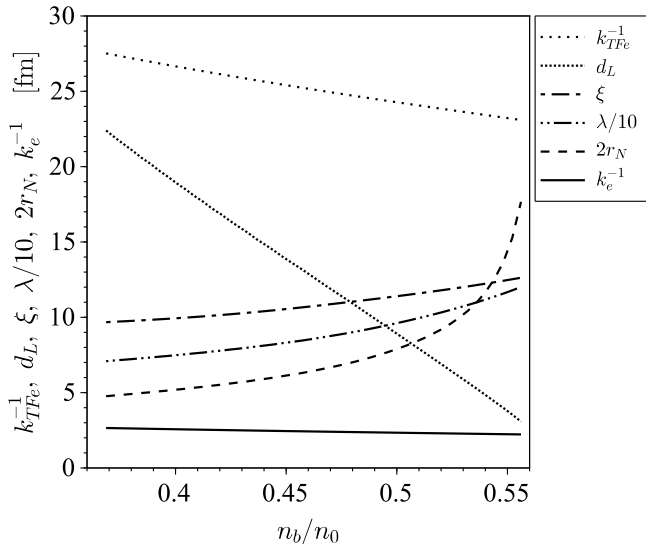


FIG. 9. The characteristic parameters of proton superconductor in 1N phase calculated from Figs. 1-4 and supplemented by the data on $\Delta_p(k_{FD})$ from Fig. 7 of [6]. The distance between the nearest interfaces of two adjacent slabs is d_L , λ is the lower bound on the London penetration depth of the magnetic field into the superconducting protons, ξ is the coherence length of protons at temperatures well below $k_B T$, $2r_N$ is the width of the slab (also given in Fig. 2), k_{TFe}^{-1} is the characteristic screening length in the electron background and k_e^{-1} is the electron Fermi wavenumber.

the superconducting density smoothly goes to zero. In the nuclear system, the normal cores are filled by the normal protons, so the sum of the superconducting and the normal proton densities is constant. There is yet another physical interpretation of ξ as characteristic size of the Cooper pair. General considerations suggest that the slab can be thought of a three-dimensional superconducting domain when size of the Cooper pair ξ is smaller than the domain width along the smallest dimension, which is $2r_N$ in case of 1N phase. When the Cooper pair ξ is larger than $2r_N$, the slab represents effectively two-dimensional system.

Another important aspect of the problem is whether the Cooper pair size ξ is smaller or larger than the spacing d_L between two adjacent slabs. If two slabs are a pair of parallel two-dimensional nuclear films separated by a distance d_L smaller than the size ξ of the Cooper pair, $d_L < \xi$, then it is natural to expect that the phase fields of the order parameter corresponding to the two slabs are synchronized *i.e.* mutually coherent. On the contrary, when $d_L > \xi$, it is natural to expect that the slabs are mutually incoherent, *i.e.* their phase fields are independent because they are separated by a locally low-density region, which contains large superconducting phase fluctuations that destroy the coherence. Therefore the results shown in Fig. 9 suggest that for $n_b \gtrsim 0.48n_0$ the slabs are coupled by the Josephson effect because $\xi > d_L$.

It is seen that the individual slabs have two-dimensional character for $n_b \lesssim 0.54n_0$, while for $n_b \gtrsim 0.54n_0$ the slabs

are effectively three-dimensional. We observe that the approach used by Zhang and Pethick in [5] is valid in the range $0.48n_0 \lesssim n_b \lesssim 0.54n_0$.

In the range $n_b \lesssim 0.48n_0$ the slabs are not significantly coupled by the Josephson effect because $\xi < d_L$. Thus, the approach used by Kobayakov in [3] is valid in the range $0.37n_0 \lesssim n_b \lesssim 0.48n_0$.

B. Natural stress of the superconducting-superfluid crust in neutron stars

In the standard astrophysical picture, neutron stars observable as pulsars are characterized by the electromagnetic emission related to rotation of the dipolar magnetic field in space because the latter is misaligned with the spinning axis. As a result, rotation of the conglomerate of charged particles inside pulsar *continuously* slows down due to the emission losses. This is not the case for the superfluid neutrons, which are expected to slow down via *abrupt* jumps of the rotation frequency due to the quantum character of the rotational energy of neutrons, namely the pinning of the superfluid neutron vortices prevents their continuous outflow and the total number of vortices changes abruptly (as a vorticity discharge) when avalanche of vortices suddenly unpins. Thus, the mutual rotational evolution of the nonsuperfluid and superfluid particles naturally includes situations when there is an adiabatic perturbation of the macroscopic flow of neutrons in the rest frame of reference of the center-of-mass of the slab. A relevant question in this case is, whether the perturbation of the neutron superflow in the magnetic field \mathbf{H} would lead to a magnetohydrodynamic stress?

Stresses of the superconducting-superfluid crust in neutron stars can be conveniently studied in the framework of the stress tensor approach. Tensor of the momentum and energy, or briefly, the stress tensor, contains information about hydrodynamic and magnetic content in the system. It is useful for studies of pressure forces and the interaction of the fluid with the magnetic field. Often, it is convenient to study the stress tensor for some specific form of motion and specific initial conditions for the magnetic field. For instance, the case that can be loosely described as magnetostatic-hydrostatic was studied by Easson and Pethick in [40], while the magnetostatic-hydrodynamic situation was studied by Sedrakian and Sedrakian in [41] in the context of the uniform nuclear matter in the core of neutron stars and later by Kobayakov in [3] in the context of nonuniform matter in the inner crust of neutron stars.

The pioneering work [40] was done for the case of a uniform isotropic superconductor threaded by the quantized magnetic flux lines, while there is no macroscopic flow of matter. In the setting utilized in [40], a virtual change in the parallelepiped leads to a perturbation of the total density of matter. Thus, in uniform neutron star matter with nucleon densities denoted by $n_p = xn$ and $n_n = (1-x)n$, the magnetic part of

the stress tensor (see Eq. (8) in [40]) reads

$$\begin{aligned} \sigma_{ij}^{\text{mag, unif}} &= \left[F^{\text{mag}} - n \left(x \frac{\partial}{\partial n_p} + (1-x) \frac{\partial}{\partial n_n} \right) F^{\text{mag}} - \frac{1}{4\pi} \mathbf{H} \cdot \mathbf{B} \right] \delta_{ij} \\ &+ \frac{1}{4\pi} H_i B_j, \end{aligned} \quad (22)$$

where F^{mag} is the magnetic part of the free energy (see Eq. (5) in [40]) defined as the piece of the total free energy F that is nonzero only when the magnetic induction is present:

$$F = F^{\text{matter}} + F^{\text{mag}}(\mathbf{B}), \quad (23)$$

and where the dependence on the matter density is implicit. Equation (22) holds independently of whether the protons are superconducting or not. The information regarding the superconductivity and the coupled superfluidity is contained inside F^{mag} .

In the following work, scenarios involving some form of a macroscopic fluid flow were studied. The approach of Sedrakian and Sedrakian [41] focused on interaction of the superconducting protons with the superfluid rotation of neutrons, which generates the magnetization due to the entrainment effect.

The intrinsic momentum coupling between superfluid neutrons and superconductor protons is a phenomenon known as the *entrainment* in the superconducting-superfluid uniform nuclear matter. The entrainment contribution to the total energy density depends on the electromagnetic vector potential \mathbf{A} through the gauge-invariant difference of the gradient of the phase of the proton superconducting order parameter $\nabla\phi_p$ and \mathbf{A} . This contribution may be understood as the one coming from the $F^{\text{mag}}(\mathbf{B})$ dependence.

As a next step, recently, effects of a macroscopic flow of superfluid neutrons in nonuniform matter of the inner crust of neutron stars were studied by Kobayakov [3]. Notice that the elastic properties are irrelevant for the aims of finding the force due to the combined action of the magnetic field and the neutron superflow in [3].

A natural feature of the inner crust matter is that the superconductor though it is still type-II, is extremely anisotropic. As it follows from our calculations, this happens at the mean baryon number density close to the tip of 1N phase, where $\xi < d_L$, see Fig. 9. This is because in 1N phase the proton supercurrents are possible only inside the nuclear slabs of the ideally ordered 1N phase and not between them via the pure neutron liquid.

In case when $\xi < d_L$, depending on the relative orientation of the structure and the applied magnetic field, the magnetic flux penetrates either in the form of a *quantized* flux tube array, as in the case shown in Fig. 8 (b), or in the form of a *non-quantized* magnetic flux through the voids between the slabs, as in the case shown in Fig. 8 (a). Notice that the magnetic induction is almost equal to the magnetic field inside the slab, because the condition

$$\frac{\lambda}{2r_N} \gg 1 \quad (24)$$

does hold for the entire domain of the 1N phase, as shows Fig. 8.

Let us turn to the special (but natural) case, when the magnetic field is parallel to the slab surface, as shows Fig. 8 (a). In this case, ignoring the anisotropy of the elastic energy and utilizing the notation used for description of the pasta phases, we find:

$$\begin{aligned} \sigma_{ij}^{\text{mag, 1N}} &= \left[F^{\text{mag}}(u, n, x, \mathbf{A}) - n_b \frac{\partial F^{\text{mag}}(u, n, x, \mathbf{A})}{\partial n_b} \right. \\ &\left. - \frac{1}{4\pi} \mathbf{H} \cdot \mathbf{B} \right] \delta_{ij} + \frac{1}{4\pi} H_i B_j, \end{aligned} \quad (25)$$

where the entrainment contribution $-\frac{1}{2}mn_{np}\mathbf{w}^2\delta_{ij}$ (introduced in Eq. (8) of [3]) is contained in $F^{\text{mag}}(u, n, x, \mathbf{A})$. The momentum lag is defined as

$$\mathbf{w} = \frac{1}{m} \left[\left(\mathbf{p}_p - \frac{e}{c} \mathbf{A} \right) - \mathbf{p}_n \right], \quad (26)$$

where $\mathbf{p}_q = \hbar\nabla\phi_q$, ($q = p, n$), with ϕ_q being the superfluid phase of the order parameters of the nucleons of type q . The entrainment contribution gives rise to a characteristic force operating when the neutron-proton lag \mathbf{w} is nonzero [3]. A brief account of the derivation of this force from the basic energy functional is given in Appendix E, where the magneto-hydrodynamic stress tensor is denoted as Π_{ij} . The expression for the force was given in Eq. (40) of [3] (see also a corrected expression in [42]).

Let us generalize the expression for the force up to the case when the magnetic induction \mathbf{B} has arbitrary angle ($\pi/2 - \theta$) with the neutron velocity perturbation. As a reminder, in [3] the angle was $\pi/2$, or equivalently $\theta = 0$. The magnetic induction \mathbf{B} is still restricted to the plane parallel to the slab surface and the momentum lag has the form

$$\mathbf{w} = \mathbf{w}_0 + \delta\mathbf{w}, \quad (27)$$

where \mathbf{w}_0 is the equilibrium value and $\delta\mathbf{w} = \delta w(\hat{\mathbf{y}}\cos\theta + \hat{\mathbf{x}}\sin\theta)$ is the perturbation. In order to find the force acting on a single slab (as shown in Fig. 8 (c)), we evaluate the perturbation of the stress tensor caused by the momentum lag perturbation in Eq. (E6), and we obtain:

$$\begin{aligned} \delta^{(1)}\mathbf{F}_{\text{tot}}^{1\text{cm}^2 \times 2r_c} &= 1\text{cm}^2 \times [P(z = r_N) - P(z = -r_N)]\hat{\mathbf{z}} \\ &= -1\text{cm}^2 \times \hat{\mathbf{z}} \frac{e}{c} B_0 2r_N n_{np0} \delta w \cos\theta, \end{aligned} \quad (28)$$

where n_{np0} is the entrainment number density inside the slab, ($\pi/2 - \theta$) is the angle between the magnetic field \mathbf{B}_0 and the vector of perturbation of the momentum lag $\delta\mathbf{w}$.

Since the slabs are independent ($\xi < d_L$), therefore the total force acting on a column of the 1N phase (as shown in Fig. 8 (a)) is given as a sum of contributions from each of the individual slabs, Eq. (E12). It is convenient to express the momentum lag in terms of the velocity lag

$$(\hat{\mathbf{y}}\cos\theta + \hat{\mathbf{x}}\sin\theta)\delta v = \mathbf{v}_p - \mathbf{v}_n, \quad (29)$$

via

$$\delta w = \frac{n_p n_{ni}}{n_{pp} n_{nn} - n_{np}^2} \delta v, \quad (30)$$

with $n_{pp} = n_p - n_{np}$ and $n_{nn} = n_{ni} - n_{np}$. In terms of the dimensionless variables used in this paper, we obtain

$$n_{pp} n_{nn} - n_{np}^2 = n_0^2 x (1-x) \eta^2 \left[1 - 2 \left(1 - \frac{m}{m_0^*} \right) \eta \right], \quad (31)$$

where m_0^* is the so called isovector effective nucleon mass defined in Eq. (E9) and

$$\eta \equiv \frac{n}{n_0}. \quad (32)$$

Combining Eqs. (28)-(31) and (E12), we obtain

$$\delta \mathbf{F}_{\text{tot}}^{1 \text{ cm}^2 \times D} = -\hat{\mathbf{z}} 2 \left(1 - \frac{m}{m_0^*} \right) D \frac{e}{c} B_0 n_0 u \frac{x(1-x) \eta^2}{1 - 2 \left(1 - \frac{m}{m_0^*} \right) \eta} \delta v. \quad (33)$$

We assume the magnetic field (which in this case is almost the same as the magnetic induction) $B_0 = 5 \times 10^{14}$ G and the velocity lag between neutrons and protons is $\delta v \sim 1 \text{ cm s}^{-1}$, which corresponds to a rotational lag between superfluid neutrons and the normal part of the star of the order of 10^{-6} s^{-1} . In this case, Eq. (33) can be written as an engineering formula:

$$\begin{aligned} \left| \delta \mathbf{F}_{\text{tot}}^{1 \text{ cm}^2 \times D} \right| &= 2.501 \times 10^{33} \text{ [dyn]} \quad (34) \\ &\times \left| 1 - \frac{m}{m_0^*} \right| u \frac{x(1-x) \eta^2}{1 - 2 \left(1 - \frac{m}{m_0^*} \right) \eta} \\ &\times \left(\frac{D}{1 \text{ cm}} \right) \left(\frac{B_0}{5 \times 10^{14} \text{ G}} \right) \left(\frac{\delta v}{1 \text{ cm s}^{-1}} \right). \end{aligned}$$

Noticing that at given n_b , u is uniquely determined by the values of n and n_{no} , and inserting the values for the variables u , n and x shown in Figs. 1-4, in Fig. 10 we plot the total force acting on a column of lasagna in the configuration shown in Figs. 8 (a), (c) for $\theta = \pi/2$, at $D = 1 \text{ cm}$, $B_0 = 5 \times 10^{14} \text{ G}$, $\delta v = 1 \text{ cm s}^{-1}$, $n_0 = 0.1561 \text{ fm}^{-3}$ and $m_0^*/m = 0.9466$.

The result presented in Fig. 10 corroborates the earlier conclusion regarding the possible magnitude of the force (see the corresponding discussion and Eq. (44) in [3]) and reveals a more detailed picture than existed earlier.

It is worth to emphasize that we have assumed $D \sim 1 \text{ cm}$ from the dimensional considerations and within the basic assumptions of the model, though likely $D \ll 1 \text{ cm}$ in the real neutron stars. As to the velocity perturbation $\delta v \sim 1 \text{ cm s}^{-1}$, its magnitude has been assumed from the observational data on pulsars, which constrain the lag of the rotational frequencies of the superfluid and nonsuperfluid components to maximum values of the order of 10^{-6} s^{-1} [52].

V. SUMMARY AND OUTLOOK

We have solved the complete set of coupled algebraic equations, Eqs. (4)–(7) to determine the equilibrium values, and

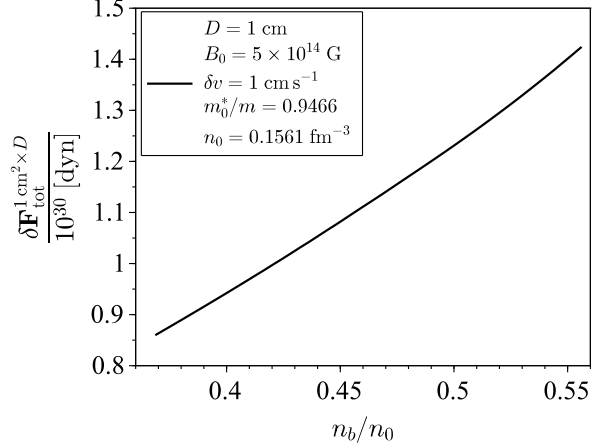


FIG. 10. Numerical evaluation of Eq. (34) in 1N phase with the variables u , n and x shown in Figs. 1-4 and with the other variables specified in the inset.

thereby the equilibrium structure in LDM, of the number density of neutrons outside the nucleus or inside the bubble n_{no} , the number density of baryons n and the proton fraction x inside the nucleus or outside the bubble, and the nucleus radius r_N or the bubble radius r_B , at given mean baryon density n_b . In this way we have calculated the energy spectrum of the hydrostatic configurations of our system that represents the neutron star matter in the inner crust.

As a novel element in our study, we have computed self-consistently at Extended Thomas-Fermi level the surface tension and the curvature correction of the interface that separates the nucleus from the pure neutron matter using the same nuclear interaction Sk χ 450 as in the calculation of the bulk, the surface and the pairing properties. We have seen in Table I that the small correction due to the curvature leads to qualitative changes in the ground state. Thus, the correction due to the curvature though it is small, is qualitatively important.

We have found that at a fixed depth in the inner crust, which is characterized by a fixed average baryon number density n_b , there is a hydrostatic configuration with the minimum energy and, depending on the depth, there are other hydrostatic configurations with slightly higher energies. Our numerical calculations, based on a realistic nuclear interaction model, have shown that the energy difference is often smaller than the thermal energy per baryon. This finding suggests that in reality, matter in the inner crust at given depth might be polymorphic and contain coexisting various phases of the pasta structures (see Fig. 6 for more details).

The results of our initial estimates of the coherence length ξ , the slab width $2r_N$, the penetration depth of the magnetic field λ and the Thomas-Fermi screening length of the electrons k_{TFe}^{-1} suggest that the magnetic properties of the 1N phase in the pasta phase are nontrivial. As seen from Fig. 9, at $n_b \sim 0.48 n_0$ there is an intersection of the line ξ representing the coherence length and the line d_L representing the distance between adjacent slabs. This implies that the characteristic

radius of the normal core of quantized magnetic fluxtube for $0.37n_0 < n_b < 0.48n_0$ is smaller than the separation between adjacent slabs and therefore the magnetic flux is nonquantized, as shown in Fig. 8 (a). As a result, dynamical evolution of the magnetic flux in the material restricted to the geometry shown in Fig. 8 (a), is not accompanied by a dissipative dynamics of the nonuniform superconducting order parameter, in contrast to the configuration shown in Fig. 8 (b), where dynamical evolution of the magnetic flux is accompanied by the dissipative motion of the flux tube which intersects the slabs.

Our calculations reported in Fig. 5 for the workfunction to transfer a proton from the nucleus to the surrounding pure neutron matter, suggest that the energy landscape for the protons and their tunneling properties are more complicated than assumed in the earlier studies [5]. Our calculations validate the approach within the anisotropic Ginzburg-Landau model used by Zhang and Pethick in [5] for the mean baryon density range corresponding to $d_L/\xi < 1$, which from Fig. 9 is at $0.48n_0 < n_b < 0.55n_0$. However, for $0.37n_0 < n_b < 0.48n_0$ the system should be described as a collection of individual two-dimensional slabs. In this case, the superconducting density is nonuniform and might be multiply-connected depending on the boundaries of the matter domains containing 1N pasta phase. Obviously, this physical situation is very different from a system where the superconducting matter is uniform and singly-connected as expected in the outer core of neutron stars.

As an astrophysical application, we have considered 1N phase in the magnetic field with a macroscopic flow of superfluid neutrons. In particular, we have studied the magneto-hydrodynamic force arising from a perturbation of the neutron velocity δv relative to the electron-proton plasma. In observable neutron stars with overlapping superfluid neutrons and protons in the interior, the superfluid lag δv develops naturally, as a result of slowing down of the charged particles together with the pinned neutron vortices and pinned flux tubes, while keeping the superfluid neutron quantum rotational state unaltered during a significant period of time due to the neutron vortex pinning.

Noticing that the superconducting-superfluid entrainment energy contribution is a part of the magnetic piece of the free energy, we have revealed the connection between the stress tensor for the mixture with entrainment [3, 41] and the stress tensor previously considered for the case of uniform isotropic superconductors [40]. In this paper we have improved the numerical evaluation of the stress tensor in the inner crust of neutron stars, by using the parameters of the 1N phase calculated from microscopic physics and reported in Figs. 1-4.

With the new, realistic, estimates obtained in this work, we have corroborated the conclusion reached earlier in [3]: The characteristic superconductor force resulting from a specific combination of the pasta structure, the magnetic field and the neutron superfluid flow, with typical physical conditions expected in neutron stars, might acquire a magnitude that is large enough to shatter the crust. In this scenario, the rotational lag between the non-superfluid and superfluid components of the star, which is built up naturally in every observable neutron

star with pinned superfluid vorticity, is a natural triggering agent for initiation of the crust shattering. The reasons that the force might acquire such a high magnitude are three-fold: (i) The non-quantized character of the magnetic flux in the configuration shown in Fig. 8 (a); (ii) a macroscopically large width D of the 1N phase; (iii) the assumption that the slabs are ideally aligned in the azimuthal direction at any longitude with fixed latitude.

It is worth saying that there are directions for further improvement of our predictions regarding the inner crust structure. First, it would be interesting to include smaller corrections such as the neutrons adsorbed on the surface of nuclei and bubbles and some others. Second, the effects of a moderate strength magnetic field ($\sim 10^{15}$ Oe) on the inner crust structure should be studied, because the energy gaps in the hydrostatic energy spectrum have been found so small and might compare with the energy associated with the magnetic flux tube and the magnetized neutron vortex.

Qualitatively, in this paper we have confirmed by the numerical calculation that the electrical conductivity in the inner crust is not purely electronic. Since we have found that a significant part of the inner crust contains the 1N phase as the ground state, it is natural to expect that macroscopic domains of matter containing the 1-dimensional should be present in real neutron star crusts. Therefore, the electrical conductivity in some macroscopic parts of the inner crust in neutron stars is due to both the normal electrons and the superconducting protons.

ACKNOWLEDGEMENTS

X.V. warmly acknowledges useful discussions with B. K. Sharma and M. Centelles. The work of D.K. reported in Secs. I-III was supported by Center of Excellence ‘‘Center of Photonics’’ sponsored by the Ministry of Science and Higher Education of Russia, contract № 075-15-2022-316. The work of D.K. reported in Sec. IV was supported by RSF project № 20-12-00268. X.V. acknowledges partial support from Grants No. PID2023-147112NB-C22 and No. CEX2019-000918-M (through the ‘‘Unit of Excellence María de Maeztu 2020-2023’’ award to ICCUB) from the Spanish MCIN/AEI/10.13039/501100011033.

Appendix A: The energy density functional and properties of uniform nuclear matter

In this work we use the Skyrme mean-field models constrained by the bulk matter equation of state computed using effective field theory and the ground-state energies of doubly magic nuclei introduced by Lim and Holt [22]. In the ETF approximation the quantum kinetic energy density is replaced by the semiclassical one [33] that at \hbar^2 order is expressed by a density functional that includes second order derivatives of the neutron proton densities. Within this approach the energy density for this kind of interactions reads:

$$\begin{aligned}
\varepsilon = & \frac{\hbar^2}{2m}(f_n \tau_n + f_p \tau_p) + \frac{t_0}{4}[(x_0 + 2)n^2 - (2x_0 + 1)(n_n^2 + n_p^2)] \\
& - \frac{1}{32}[t_2(2 + x_2) - 3t_1(2 + x_1)](\nabla n)^2 - \frac{1}{32}[3t_1(2x_1 + 1) + t_2(2x_2 + 1)][(\nabla n_n)^2 + (\nabla n_p)^2] \\
& + \frac{t_3 n^{\alpha_1}}{24}[(x_3 + 2)n^2 - (2x_3 + 1)(n_n^2 + n_p^2)] + \frac{t_4 n^{\alpha_2}}{24}[(x_4 + 2)n^2 - (2x_4 + 1)(n_n^2 + n_p^2)] \\
& - \frac{W_0}{2}(n \nabla \cdot \mathbf{J} + n_n \nabla \cdot \mathbf{J}_n + n_p \nabla \cdot \mathbf{J}_p)
\end{aligned} \tag{A1}$$

where f_q ($q = n, p$) is the inverse of the nucleon *effective mass* for each nucleon species, which is defined as

$$f_q = \frac{m}{\bar{m}_q} = 1 + \frac{m}{4\hbar^2} \{ [t_1(x_1 + 2) + t_2(x_2 + 2)]n + [t_2(2x_2 + 1) - t_1(2x_1 + 1)]n_q \}. \tag{A2}$$

Here, τ_q and \mathbf{J}_q are the \hbar^2 -order ETF kinetic energy density and the spin densities, respectively, which read

$$\tau_q = \frac{3}{5}(3\pi^2)^{2/3} n_q^{5/3} + \frac{1}{36} \frac{(\nabla n_q)^2}{n_q} - \frac{1}{3} \frac{\nabla f_q \nabla n_q}{f_q} - \frac{1}{12} n_q \frac{(\nabla f_q)^2}{f_q^2} + \frac{(\mathbf{J}_q)^2}{2n_q} \quad \text{and} \quad \mathbf{J}_q = \frac{m}{\hbar^2} W_0 \frac{n_q}{f_q} (\nabla n + \nabla n_q) \tag{A3}$$

In the LDM calculations the relevant part of the energy density functional (A1) is the bulk part, which we write in a dimensionless form by scaling the energies and densities by the Fermi energy ε_0 and the saturation density, respectively. Map-

ping of the operator form of the interaction energy from Eqs. (3)-(4) of [22] to the energy per baryon ε in uniform nuclear matter can be done using the formula given by Eq. (1) of [44], leading to:

$$\begin{aligned}
\varepsilon(n, x) = & \frac{3}{5} \varepsilon_0 (2\eta)^{2/3} \left\{ \left[x^{5/3} + (1-x)^{5/3} \right] \left(1 + \frac{\tilde{a}}{8} \eta \right) + \left[x^{8/3} + (1-x)^{8/3} \right] \frac{\tilde{b}}{4} \eta \right\} \\
& + \frac{t_0 n_0}{4} \eta \{ x_0 + 2 - (2x_0 + 1) [x^2 + (1-x)^2] \} \\
& + \frac{t_3 n_0^{\alpha_1 + 1}}{24} \eta^{\alpha_1 + 1} \{ x_3 + 2 - (2x_3 + 1) [x^2 + (1-x)^2] \} \\
& + \frac{t_4 n_0^{\alpha_2 + 1}}{24} \eta^{\alpha_2 + 1} \{ x_4 + 2 - (2x_4 + 1) [x^2 + (1-x)^2] \},
\end{aligned} \tag{A4}$$

where $\eta \equiv n/n_0$,

$$\tilde{a} = \frac{2m_p}{\hbar^2} n_0 [t_1(x_1 + 2) + t_2(x_2 + 2)], \tag{A5}$$

$$\tilde{b} = \frac{2m_p}{\hbar^2} n_0 [t_2(2x_2 + 1) - t_1(2x_1 + 1)], \tag{A6}$$

and the numerical values of the parameters are given in Table II. The critical density at which the uniform nuclear matter becomes unstable with respect to hydrostatic perturbations is

$$\eta_{\text{uni}}^* \equiv n_t/n_0, \tag{A7}$$

with n_t given by Eq. (30) of [22].

The nuclear saturation condition expresses the fact that the symmetric nuclear matter at saturation is pressureless:

$$P_{\text{nuc}}(n = n_0, x = 1/2) = 0. \tag{A8}$$

The nuclear binding energy per nucleon is given by

$$B = \varepsilon(n = n_0, x = 1/2). \tag{A9}$$

The nuclear symmetry energy is defined as

$$S = \varepsilon(n = n_0, x = 0) - \varepsilon(n = n_0, x = \frac{1}{2}) \tag{A10}$$

and its slope parameter

$$L = \frac{3}{8} n_0 \partial_{nxx}^3 \varepsilon|_{n=n_0, x=1/2}. \tag{A11}$$

The incompressibility is given by

$$K = 9 \partial_n^3 P_{\text{nuc}}|_{n=n_0, x=1/2}. \tag{A12}$$

The parameters K and S have been constrained by the experiment: the expected range of K is 230 ± 30 MeV and the expected range of S is 32 ± 2 MeV [45]. However, the slope parameter L is not well constrained as various models predict different values of L . For instance, the Skyrme interactions favored in [44] predict L in the range between 53.04 and 61.45 MeV; the chiral effective field theory predictions reported in [46, 47] span the range between 36.5 and 69.0 MeV. A recent review is given in [48].

t_0	-1803.2928
t_1	301.8208
t_2	-273.2827
t_3	12783.8619
t_4	564.1049
x_0	0.4430
x_1	-0.3622
x_2	-0.4105
x_3	0.6545
x_4	-11.3160
α_1	1/3
α_2	1
n_0	0.1561141
P_{nuc}^*	3×10^{-6}
B	-15.91
K	239.3
S	31.44
L	42.07

TABLE II. Nuclear interaction parameters are given by $t_{0,1,2,3,4}$, $x_{0,1,2,3,4}$, $\alpha_{1,2}$ [22]. The empirical nuclear parameters B , K , S , L have the dimension of MeV and are calculated from Eqs. (A9)-(A12). The physical dimensions: t_0 is in MeV fm³, $t_{1,2}$ are in MeV fm⁵, $x_{0,1,2,3,4}$, q and α are dimensionless, t_3 is in MeV fm^{3(α_1+1)} and t_4 is in MeV fm^{3(α_2+1)}. The nuclear symmetric saturation density n_0 (measured in fm⁻³) is fine-tuned so that the empirical condition for the pressure (P_{nuc} is in MeV fm⁻³), Eq. (A8), is satisfied to a good precision.

Appendix B: Nuclear clusters in LDM

The independent variables of the compressible liquid drop model for the nuclei are

$$\{n_b, n, x, r_N, n_{no}, n_{sk}, n_{dc}\}. \quad (\text{B1})$$

In the practical problem, the average baryon density n_b is fixed. Thus, the unknown variables are

$$\{n, x, r_N, n_{no}, n_{sk}, n_{dc}\}. \quad (\text{B2})$$

The definition of the variables is given below.

1. Energy density

The protons are uniformly distributed within the nucleus with volume V_N with the number density

$$n_p = \frac{N_p}{V_N}. \quad (\text{B3})$$

Here,

$$V_N = \begin{cases} (4/3)\pi r_N^3, & (3N) \\ \pi r_N^2 \times L, & (2N) \\ 2r_N \times L^2, & (1N) \end{cases} \quad (\text{B4})$$

where r_N is the radius of the nucleus, $L \rightarrow \infty$ is the length of the rod-like nucleus and $L^2 \rightarrow \infty$ is the area of the slab-like nucleus, see Fig. 11 (b). Here, $L \rightarrow \infty$ should be understood as large enough L so that the Coulomb energy per unit length or area of nuclei and bubbles does not depend on L .

The nucleus volume fraction is

$$u = \frac{V_N}{V_c} = \left(\frac{r_N}{r_c}\right)^d, \quad (\text{B5})$$

where r_c is the radius of the unit cell and d is the dimensionality ($d = 3$ for 3N, $d = 2$ for 2N and $d = 1$ for 1N). The volume of the unit cell is

$$V_c = \begin{cases} (4/3)\pi r_c^3, & (3N) \\ \pi r_c^2 \times L, & (2N) \\ 2r_c \times L^2, & (1N) \end{cases} \quad (\text{B6})$$

Neutrons, however, are distributed within the entire cell: In the nucleus and in the volume of the cell excluding the volume of the nucleus. Moreover, there are neutrons adsorbed on the surface of the nucleus associated with the neutron skin and associated with the density curvature, *i.e.* the region where the second spatial derivative of the nucleon number density with respect to the coordinate normal to the nucleus surface is nonzero.

Thus, the total number of neutrons in the cell can be split into three parts:

$$N_n = N_{ni} + N_{surf} + N_{no}, \quad (\text{B7})$$

which corresponds to neutrons inside the nucleus, at the surface and outside the nucleus. We define the following neutron number densities.

The *local* number density of neutrons inside the nucleus is

$$n_{ni} = \frac{N_{ni}}{V_N} = (1-x)n, \quad (\text{B8})$$

where we introduce the standard definition of the proton fraction,

$$x = \frac{N_p}{N_p + N_{ni}} \quad (\text{B9})$$

and of the baryon density inside the nucleus

$$n = \frac{N_p + N_{ni}}{V_N}. \quad (\text{B10})$$

The *local* number density of neutrons outside the nucleus is

$$n_{no} = \frac{N_{no}}{V_c - V_N}. \quad (\text{B11})$$

The surface neutrons (adsorbed on the surface of the nucleus) can be represented as neutrons associated with the neutron skin and with the surface width (the density curvature):

$$N_{surf} = N_{sk} + N_{dc}. \quad (\text{B12})$$

The *cell-averaged* number density of the skin neutrons is

$$n_{sk} = \frac{N_{sk}}{V_c}. \quad (\text{B13})$$

The *cell-averaged* number density of neutrons associated with the density curvature is

$$n_{dc} = \frac{N_{dc}}{V_c}. \quad (\text{B14})$$

Derivation of the governing variational equations of LDM assumes that n_{sk} and n_{dc} are independent variables. It is important that as soon as the variational equations are derived, the quantities n_{sk} and n_{dc} can be specified from the microscopic equations of the Skyrme model as following:

$$n_{sk} = \begin{cases} 4\pi r_N^2 s_n (n_L - n_G) V_c^{-1}, & (3N) \\ 2\pi r_N s_n (n_L - n_G) V_c^{-1} \times L, & (2N) \\ s_n (n_L - n_G) V_c^{-1} \times L^2, & (1N) \end{cases} \quad (\text{B15})$$

where $s_n = s_n(x)$ is the neutron skin thickness, and

$$n_{dc} = \begin{cases} 8\pi r_N (b_n^2 - b_p^2 + s_n^2) (n_L - n_G) V_c^{-1}, & (3N) \\ 2\pi (b_n^2 - b_p^2 + s_n^2) (n_L - n_G) V_c^{-1} \times L, & (2N) \\ 0, & (1N) \end{cases} \quad (\text{B16})$$

where $b_n = b_n(x)$, $b_p = b_p(x)$ are the neutron surface width, proton surface width and $n_L = n_L(x)$ and $n_G = n_G(x)$ are some parameters; these quantities will be explicitly presented elsewhere.

Consequently, the *cell-averaged* number density of baryons can be written as

$$n_b = un + (1-u)n_{no} + n_{sk} + n_{dc}. \quad (\text{B17})$$

As we have defined the necessary ingredients, we turn to defining the total energy density

$$w_{\text{tot}} = \frac{E_{\text{tot}}}{V_c}. \quad (\text{B18})$$

In LDM, the total energy density includes contributions to the energy per baryon, which we choose to express by the following 8 terms:

$$\begin{aligned} w_{\text{tot}} & \\ &= w_{\text{nuc}} + w_{\text{p.surf}} + w_{\text{C+L}} + w_{\text{no}} + w_e + w_{\text{curv}} + w_{\text{sk}} + w_{\text{dc}}. \end{aligned} \quad (\text{B19})$$

where w_{nuc} is the bulk (uniform) energy density of the nuclear cluster. The terms $w_{\text{p.surf}}$ and w_{curv} are the nuclear surface contributions (from the *planar surface* and from the *curvature*). The contribution from the dripped neutron liquid is given by w_{no} and the kinetic energy of the electron background by w_e . The Coulomb energy term $w_{\text{C+L}}$, collects the self-energy of protons in the nuclear cluster and of electrons distributed in the WS cell as well as the proton-electron lattice energy. Finally, the w_{sk} and w_{dc} provide the neutron energy due to neutrons accumulated at the surface of the nuclear cluster, being

the former the contribution from the planar interface and the latter the correction due to its curvature.

The rest mass contribution due to baryons and the strong interaction contribution associated with the uniform matter inside the nucleus is given by

$$w_{\text{nuc}} = un [(1-x)m_n + xm_p]c^2 + un\mathcal{E}(n,x), \quad (\text{B20})$$

where m_p and m_n are the proton and neutron rest masses, correspondingly, c is the speed of light and \mathcal{E} is the energy per baryon specified in the Appendix.

The planar surface energy density $w_{\text{p.surf}}$ is proportional to the surface area of the nucleus and therefore has the form

$$w_{\text{p.surf}} = \frac{ud}{r_N} \sigma_s(x), \quad (\text{B21})$$

where $\sigma_s(x)$ is a function with dimension MeV fm⁻² and is computed by the method described in [34] with the results presented in Appendix D. The Coulomb energy density including the nucleus self-energy and the lattice energy is [18, 49]

$$w_{\text{C+L}} = 2\pi(enxr_N)^2 u f_d(u), \quad (\text{B22})$$

where

$$f_d(u) = \frac{1}{d+2} \left[\frac{2}{d-2} \left(1 - \frac{du^{1-2/d}}{2} \right) + u \right], \quad (\text{B23})$$

with

$$\begin{aligned} f_3(u) &= \frac{1}{5}(2 - 3u^{1/3} + u), \\ f_2(u) &= \frac{1}{4} \left(\ln \frac{1}{u} - 1 + u \right), \\ f_1(u) &= \frac{1}{3} \left(\frac{1}{u} - 2 + u \right). \end{aligned}$$

Equation (B22) describes a sum of electrostatic energy of a single cluster plus energy of interaction of the cluster with the lattice of other cluster plus the correction due to the finite size of the cluster [49]. The energy density of the dripped neutrons w_{no} is

$$w_{\text{no}} = (1-u)n_{no} [m_n c^2 + \mathcal{E}(n_{no}, 0)], \quad (\text{B24})$$

the electron energy density w_e is

$$w_e = \frac{3}{4} \hbar c (3\pi^2)^{1/3} (unx)^{4/3}, \quad (\text{B25})$$

where we have used the electrical neutrality condition in the unit cell, so the electron number density n_e is given by

$$n_e = unx. \quad (\text{B26})$$

The energy density associated with curvature of the thin surface of nuclear matter inside the nucleus for convenience can be called the curvature energy density w_{curv} . This curvature energy density is proportional to both the surface area of the nucleus and to the mean principal curvature of the surface

of the nucleus, which is $2/r_N$ for 3D clusters, $1/r_N$ for 2D clusters and 0 for 1D clusters. Thus, it has the form

$$w_{\text{curv}} = \frac{ud(d-1)}{r_N^2} \sigma_c, \quad (\text{B27})$$

where $\sigma_c = \sigma_c(x)$ is a parameter with dimension MeV fm^{-1} and can be found using the method of [34].

The energy density associated with the neutron skin can be written as

$$w_{\text{sk}} = n_{\text{sk}} \mu_{\text{sk}}, \quad (\text{B28})$$

where μ_{sk} is defined by the variational equation with respect to n_{sk} .

Analogously, the energy density associated with the nuclear density curvature can be written as

$$w_{\text{dc}} = n_{\text{dc}} \mu_{\text{dc}}, \quad (\text{B29})$$

where μ_{dc} is defined by the variational equation with respect to n_{dc} . This term is associated with the spatial curvature of the nuclear density related to the finite width of the nucleus surface.

2. Variational equations

The variational equations have the form

$$\frac{\partial w_{\text{tot}}}{\partial y} = 0, \quad (\text{B30})$$

where y is either of the variables from the set $\{n, x, n_{\text{no}}, r_N, u, n_{\text{sk}}, n_{\text{dc}}\}$. In order to reveal the physical significance of the variational equations we shall discuss in detail each of the equations.

3. Optimum size of nucleus

The derivative

$$\left. \frac{\partial(w_{\text{tot}})}{\partial r_N} \right|_{n, x, n_{\text{no}}, u, n_{\text{sk}}, n_{\text{dc}}} = 0 \quad (\text{B31})$$

with respect to the nucleus size r_N at fixed $\{n, x, n_{\text{no}}, u, n_{\text{sk}}, n_{\text{dc}}\}$ implies that the energy per baryon is minimized by nucleus size while the number densities are fixed. Application of the derivative to Eq. (B18) yields the result known as the nuclear virial theorem with a correction due to the principal curvature of the thin surface of the dense (nuclear) phase of the inner crust matter:

$$w_{\text{p.surf}} + 2w_{\text{curv}} = 2w_{\text{C+L}}. \quad (\text{B32})$$

Notice that there are no contributions from w_{sk} and w_{dc} . From Eq. (B32) we find the equation that determines r_N :

$$r_N^4 - 4qr_N - 3r = 0, \quad (\text{B33})$$

where

$$q = \frac{1}{4} \frac{\sigma_s(x)d}{4\pi(enx)^2 f_d(u)}, \quad (\text{B34})$$

$$r = \frac{1}{3} \frac{2d(d-1)\sigma_c(x)}{4\pi(enx)^2 f_d(u)}. \quad (\text{B35})$$

The solution to Eq. (B33) can be readily found using the methods of Ferrari and Cardano resulting in

$$r_N = \sqrt{\frac{p}{2}} \left[1 + \sqrt{q \left(\frac{2}{p} \right)^{3/2} - 1} \right], \quad (\text{B36})$$

where

$$p = \left[q^2 + \sqrt{q^4 + r^3} \right]^{1/3} - \left[\sqrt{q^4 + r^3} - q^2 \right]^{1/3}. \quad (\text{B37})$$

In case when the curvature contribution is neglected one obtains a simple result,

$$r_N = \left[\frac{\sigma_s(x)d}{4\pi(enx)^2 f_d(u)} \right]^{1/3}. \quad (\sigma_c = 0) \quad (\text{B38})$$

4. Chemical equilibrium

The derivative

$$\left. \frac{\partial(w_{\text{tot}})}{\partial x} \right|_{n, n_{\text{no}}, r_N, u, n_{\text{sk}}, n_{\text{dc}}} = 0 \quad (\text{B39})$$

implies that the isospin of nucleus is in equilibrium with respect to weak interactions:

$$\mu_e + (m_p - m_n)c^2 = - \left. \frac{\partial \mathcal{E}}{\partial x} \right|_n \quad (\text{B40})$$

$$- \frac{1}{un} \left. \frac{\partial(w_{\text{p.surf}} + w_{\text{C+L}} + w_{\text{curv}})}{\partial x} \right|_{n, n_{\text{no}}, r_N, u, n_{\text{sk}}, n_{\text{dc}}}.$$

Notice that there are no contributions from w_{sk} and w_{dc} . Here, the electron chemical potential μ_e is:

$$\mu_e = \frac{1}{un} \left. \frac{\partial w_e}{\partial x} \right|_{n, n_{\text{no}}, r_N, u, n_{\text{sk}}, n_{\text{dc}}} = \hbar c (3\pi^2 un)^{1/3}. \quad (\text{B41})$$

The chemical equilibrium condition can be written as

$$\mu_e = \mu_{ni} - \mu_{pi}, \quad (\text{B42})$$

where the neutron and the proton chemical potentials are given below by Eqs. (B49) and (B53), respectively.

5. Continuity of neutron chemical potential across the nucleus interface

The derivative

$$\left. \frac{\partial(w_{\text{tot}})}{\partial n_{ni}} \right|_{N_n, n_{pi}, r_N, u, n_{sk}, n_{dc}} = 0 \quad (\text{B43})$$

implies that the total energy density is minimized by choosing the optimal number of neutrons inside and outside of the nucleus while keeping their total number fixed as well as fixing the proton number, the size of the nucleus and that of the unit cell. As a result, the energy to add a neutron to the nucleus is equal to the energy to add a neutron to the dripped neutrons, $\mu_{ni} = \mu_{no}$.

To obtain the explicit form of this condition we note that fixing of N_n, n_{pi}, r_N, u induces the following relations:

$$n\delta x + x\delta n = 0, \quad (\text{B44})$$

$$u\delta n_{ni} + (1-u)\delta n_{no} = 0. \quad (\text{B45})$$

The partial derivative is given by:

$$\begin{aligned} \frac{\partial}{\partial n_{ni}} \Big|_{N_n, n_{pi}, r_N, u, n_{sk}, n_{dc}} &= \\ \frac{\partial}{\partial n} \Big|_{x, n_{no}, r_N, u, n_{sk}, n_{dc}} + \frac{\delta n}{\delta x} \frac{\partial}{\partial x} \Big|_{n, n_{no}, r_N, u, n_{sk}, n_{dc}} & \\ + \frac{\delta n_{no}}{\delta n_{ni}} \frac{\partial}{\partial n_{no}} \Big|_{n, x, r_N, u, n_{sk}, n_{dc}} &. \end{aligned} \quad (\text{B46})$$

Using Eqs. (B44) and (B45), we find

$$\begin{aligned} \frac{\partial}{\partial n_{ni}} \Big|_{N_n, n_{pi}, r_N, u, n_{sk}, n_{dc}} &= \\ \frac{\partial}{\partial n} \Big|_{x, n_{no}, r_N, u, n_{sk}, n_{dc}} - \frac{x}{n} \frac{\partial}{\partial x} \Big|_{n, n_{no}, r_N, u, n_{sk}, n_{dc}} & \\ - \frac{u}{1-u} \frac{\partial}{\partial n_{no}} \Big|_{n, x, r_N, u, n_{sk}, n_{dc}} &. \end{aligned} \quad (\text{B47})$$

Application of these partial derivatives in Eq. (B43) yields the promised result,

$$\mu_{ni} = \mu_{no}, \quad (\text{B48})$$

where

$$\begin{aligned} \mu_{ni} = m_n c^2 + \left(\frac{\partial}{\partial n} \Big|_x - \frac{x}{n} \frac{\partial}{\partial x} \Big|_n \right) [n\mathcal{E}(n, x)] \\ - \frac{x}{un} \frac{\partial (w_{p,\text{surf}} + w_{\text{curv}})}{\partial x} \Big|_{r_N, u, n_{sk}, n_{dc}}, \end{aligned} \quad (\text{B49})$$

and

$$\begin{aligned} \mu_{no} &= \frac{1}{1-u} \frac{\partial w_{no}}{\partial n_{no}} \Big|_u \\ &= m_n c^2 + \frac{\partial}{\partial n_{no}} [n_{no}\mathcal{E}(n_{no}, 0)]. \end{aligned} \quad (\text{B50})$$

Notice that Eqs. (B49) and (B50) do not contain the contribution from w_{C+L} by virtue of Eq. (B44). Moreover, there are no contributions from w_{sk} and w_{dc} . The derivatives within μ_{ni} are calculated as following:

$$-\frac{x}{un} \frac{\partial w_{p,\text{surf}}}{\partial x} = -\frac{xd}{nr_N} \frac{\partial \sigma_s(x)}{\partial x}, \quad (\text{B51})$$

$$-\frac{x}{un} \frac{\partial w_{\text{curv}}}{\partial x} = -\frac{xd(d-1)}{nr_N^2} \frac{\partial \sigma_c(x)}{\partial x}. \quad (\text{B52})$$

By combining Eqs. (B40), (B42) and (B49) we find the proton chemical potential inside the nucleus including the surface and Coulomb corrections:

$$\begin{aligned} \mu_{pi} = m_p c^2 + \left(\frac{\partial}{\partial n} \Big|_x + \frac{1-x}{n} \frac{\partial}{\partial x} \Big|_n \right) [n\mathcal{E}(n, x)] \\ + \frac{1-x}{un} \frac{\partial (w_{p,\text{surf}} + w_{\text{curv}})}{\partial x} \Big|_{r_N, u, n_{sk}, n_{dc}} \\ + \frac{1}{un} \frac{\partial (w_{C+L})}{\partial x} \Big|_{n, r_N, u, n_{sk}, n_{dc}}. \end{aligned} \quad (\text{B53})$$

The proton chemical potential outside the nucleus can be found directly from the bulk properties of the pure neutron matter:

$$\mu_{po} = \left[\left(\frac{\partial}{\partial n} \Big|_x + \frac{1}{n} \frac{\partial}{\partial x} \Big|_n \right) [n\mathcal{E}(n, x)] \right] \Big|_{n=n_{no}, x=0}. \quad (\text{B54})$$

6. Continuity of pressure across the nucleus interface

The derivative

$$\frac{\partial (w_{\text{tot}})}{\partial u} \Big|_{N_n, N_{no}, x, V_c, n_{sk}, n_{dc}} = 0 \quad (\text{B55})$$

implies that the energy density is minimized by choosing the optimal size of the nucleus while keeping fixed the cell size, the number of neutrons inside the nucleus, the number of neutrons outside the nucleus and the proton fraction. As a result, the pressure in the nucleus is equal to the pressure in the dripped neutrons, $P_i = P_o$.

Fixing N_n, N_{no}, x and V_c induces the following relations:

$$n\delta u + u\delta n = 0, \quad (\text{B56})$$

$$(1-u)\delta n_{no} - n_{no}\delta u = 0. \quad (\text{B57})$$

The partial derivative is given by:

$$\begin{aligned} \frac{\partial}{\partial u} \Big|_{N_n, N_{no}, x, V_c, n_{sk}, n_{dc}} &= \\ \frac{\partial}{\partial u} \Big|_{n, x, n_{no}, V_c, n_{sk}, n_{dc}} + \frac{\delta n}{\delta u} \frac{\partial}{\partial n} \Big|_{n_{no}, x, r_N, u, n_{sk}, n_{dc}} & \\ + \frac{\delta n_{no}}{\delta u} \frac{\partial}{\partial n_{no}} \Big|_{n, x, r_N, u, n_{sk}, n_{dc}} &. \end{aligned} \quad (\text{B58})$$

Using Eqs. (B56) and (B57), we find

$$\begin{aligned} \frac{\partial}{\partial u} \Big|_{N_n, N_{no}, x, V_c, n_{sk}, n_{dc}} &= \\ \frac{\partial}{\partial u} \Big|_{n, x, n_{no}, V_c, n_{sk}, n_{dc}} - \frac{n}{u} \frac{\partial}{\partial n} \Big|_{n_{no}, x, r_N, u, n_{sk}, n_{dc}} & \\ + \frac{n_{no}}{1-u} \frac{\partial}{\partial n_{no}} \Big|_{n, x, r_N, u, n_{sk}, n_{dc}} &. \end{aligned} \quad (\text{B59})$$

Application of these partial derivatives in Eq. (B55) yields the promised result:

$$P_i = P_o, \quad (\text{B60})$$

where

$$P_i = n^2 \frac{\partial \mathcal{E}}{\partial n} \Big|_x - \left(\frac{\partial}{\partial u} \Big|_{n,x,n_{no},V_c,n_{sk},n_{dc}} - \frac{n}{u} \frac{\partial}{\partial n} \Big|_{n_{no},r_N,u,n_{sk},n_{dc}} \right) \times (w_{p,\text{surf}} + w_{C+L} + w_{\text{curv}}), \quad (\text{B61})$$

and

$$P_o = \frac{n_{no}}{1-u} \frac{\partial w_{no}}{\partial n_{no}} \Big|_{u,n_{sk},n_{dc}} - \frac{w_{no}}{1-u} = n_{no}^2 \frac{\partial \mathcal{E}(n_{no}, 0)}{\partial n_{no}}. \quad (\text{B62})$$

Notice that there are no contributions from w_{sk} and w_{dc} . With the help of Eq. (B56) and the relations

$$\partial(u/r_N)/\partial u|_{V_c} = (d-1)/r_N d, \quad (\text{B63})$$

$$\partial(u/r_N^2)/\partial u|_{V_c} = (d-2)/r_N^2 d, \quad (\text{B64})$$

$$\partial(r_N^2)/\partial u|_{V_c} = 2r_N^2/ud, \quad (\text{B65})$$

the derivatives within P_i are calculated as following:

$$\frac{\partial w_{p,\text{surf}}}{\partial u} \Big|_{N_n, N_{no}, x, V_c, n_{sk}, n_{dc}} = \frac{d-1}{r_N} \sigma_s(x), \quad (\text{B66})$$

$$\frac{\partial w_{\text{curv}}}{\partial u} \Big|_{N_n, N_{no}, x, V_c, n_{sk}, n_{dc}} = \frac{(d-2)(d-1)}{r_N^2} \sigma_c(x), \quad (\text{B67})$$

and

$$\left(\frac{\partial}{\partial u} \Big|_{n,x,n_{no},V_c,n_{sk},n_{dc}} - \frac{n}{u} \frac{\partial}{\partial n} \Big|_{n_{no},r_N,u,n_{sk},n_{dc}} \right) w_{C+L} = 2\pi(exnr_N)^2(u-1)g_d, \quad (\text{B68})$$

where $g_3 = 2/15$, $g_2 = 1/4$ and $g_1 = 2/3$.

7. Optimal energy to add neutron to the skin or to the density curvature region

The condition

$$\frac{\partial(E_{\text{tot}}/V_c)}{\partial n_{sk}} \Big|_{n,x,N_n,r_N,u,n_{dc}} = 0 \quad (\text{B69})$$

implies that the energy density is minimized by the optimal value of the neutrons in the *skin* while keeping $(N_{sk} + N_{no})$ fixed. This condition induces the following relation:

$$\delta n_{sk} + (1-u)\delta n_{no} = 0. \quad (\text{B70})$$

The partial derivative is given by

$$\frac{\partial}{\partial n_{sk}} \Big|_{n,x,N_n,r_N,u,n_{dc}} = \frac{\partial}{\partial n_{sk}} \Big|_{n,x,n_{no},V_c,n_{dc}} + \frac{\partial}{\partial n_{no}} \Big|_{n,x,V_c,n_{sk},n_{dc}}. \quad (\text{B71})$$

Analogously, the condition

$$\frac{\partial(E_{\text{tot}}/V_c)}{\partial n_{dc}} \Big|_{n,x,N_n,r_N,u,n_{sk}} = 0 \quad (\text{B72})$$

implies that the energy density is minimized by the optimal value of the neutrons in the *density curvature region* while keeping $(N_{dc} + N_{no})$ fixed. This condition induces the following relation:

$$\delta n_{dc} + (1-u)\delta n_{no} = 0. \quad (\text{B73})$$

The partial derivative is given by

$$\frac{\partial}{\partial n_{dc}} \Big|_{n,x,N_n,r_N,u,n_{sk}} = \frac{\partial}{\partial n_{dc}} \Big|_{n,x,n_{no},V_c,n_{sk}} + \frac{\partial}{\partial n_{no}} \Big|_{n,x,V_c,n_{sk},n_{dc}}. \quad (\text{B74})$$

Application of these partial derivatives to Eqs. (C65) and (C66) yields

$$\mu_{sk} = \mu_{no}, \quad (\text{B75})$$

$$\mu_{dc} = \mu_{no}. \quad (\text{B76})$$

Appendix C: Nuclear bubbles in LDM

The independent variables of LDM for the bubble phases are

$$\{n_b, n, x, r_B, n_{no}, n_{sk}^{\text{bub}}, n_{dc}^{\text{bub}}\}, \quad (\text{C1})$$

where the baryon density and the proton fraction outside the bubble n and x , correspondingly, the bubble radius r_B , the neutron skin density n_{sk}^{bub} and the curvature density n_{dc}^{bub} are defined below. As in the case with nuclear clusters, in the practical problem the unknown variables are:

$$\{n, x, r_B, n_{no}, n_{sk}^{\text{bub}}, n_{dc}^{\text{bub}}\}, \quad (\text{C2})$$

1. Energy density

The protons are uniformly distributed outside the bubble with volume V_B with the number density

$$n_p = \frac{N_p}{V_c - V_B}. \quad (\text{C3})$$

Here,

$$V_B = \begin{cases} (4/3)\pi r_B^3, & (3B) \\ \pi r_B^2 \times L, & (2B) \\ 2r_B \times L^2, & (1B) \end{cases} \quad (\text{C4})$$

where r_B is the radius of the bubble, $L \rightarrow \infty$ is the length of the rod-like bubble and $L^2 \rightarrow \infty$ is the area of the slab-like bubble.

The bubble volume fraction is

$$u^{\text{bub}} = \frac{V_B}{V_c} = \left(\frac{r_B}{r_c}\right)^d, \quad (\text{C5})$$

where r_c is the radius of the unit cell and d is the dimensionality ($d = 3$ for 3B, $d = 2$ for 2B and $d = 1$ for 1B). The volume of the unit cell is

$$V_c = \begin{cases} (4/3)\pi r_c^3, & (\text{3B}) \\ \pi r_c^2 \times L, & (\text{2B}) \\ 2r_c \times L^2, & (\text{1B}) \end{cases} \quad (\text{C6})$$

The total number of neutrons in the cell can be split into three parts:

$$N_n = N_{ni} + N_{surf} + N_{no}, \quad (\text{C7})$$

which corresponds to neutrons outside the bubble, at the surface and inside the bubble. We define the following neutron number densities.

The *local* number density of neutrons outside the bubble is

$$n_{ni} = \frac{N_{ni}}{V_c - V_B} = (1-x)n, \quad (\text{C8})$$

where we introduce the standard definition of the proton fraction,

$$x = \frac{N_p}{N_p + N_{ni}} \quad (\text{C9})$$

and of the baryon density outside the bubble

$$n = \frac{N_p + N_{ni}}{V_c - V_B}. \quad (\text{C10})$$

The *local* number density of neutrons inside the bubble is

$$n_{no} = \frac{N_{no}}{V_B}. \quad (\text{C11})$$

The surface neutrons (adsorbed on the surface of the nucleus) can be represented as neutrons associated with the neutron skin and with the surface width (the density curvature):

$$N_{surf} = N_{sk} + N_{dc}. \quad (\text{C12})$$

The *cell-averaged* number density of the skin neutrons is

$$n_{sk}^{\text{bub}} = \frac{N_{sk}}{V_c}. \quad (\text{C13})$$

The *cell-averaged* number density of neutrons associated with the density curvature is

$$n_{dc}^{\text{bub}} = \frac{N_{dc}}{V_c}. \quad (\text{C14})$$

Derivation of the governing variational equations of LDM assumes that n_{sk}^{bub} and n_{dc}^{bub} are independent variables. It is important that as soon as the variational equations are derived,

the quantities n_{sk}^{bub} and n_{dc}^{bub} can be specified from the microscopic equations of the Skyrme model as following:

$$n_{sk}^{\text{bub}} = \begin{cases} 4\pi r_B^2 s_n (n_L - n_G) V_c^{-1}, & (\text{3B}) \\ 2\pi r_B s_n (n_L - n_G) V_c^{-1} \times L, & (\text{2B}) \\ s_n (n_L - n_G) V_c^{-1} \times L^2, & (\text{1B}) \end{cases} \quad (\text{C15})$$

where $s_n = s_n(x)$ is the neutron skin thickness, and

$$n_{dc}^{\text{bub}} = \begin{cases} 8\pi r_B (b_n^2 - b_p^2 + s_n^2) (n_L - n_G) V_c^{-1}, & (\text{3B}) \\ 2\pi (b_n^2 - b_p^2 + s_n^2) (n_L - n_G) V_c^{-1} \times L, & (\text{2B}) \\ 0, & (\text{1B}) \end{cases} \quad (\text{C16})$$

where $b_n = b_n(x)$, $b_p = b_p(x)$ are the neutron surface width, proton surface width and $n_L = n_L(x)$ and $n_G = n_G(x)$ are some parameters, which can be found from the Skyrme model and will be presented elsewhere.

Consequently, the *cell-averaged* number density of baryons can be written as

$$n_b = (1 - u^{\text{bub}})n + u^{\text{bub}}n_{no} + n_{sk}^{\text{bub}} + n_{dc}^{\text{bub}}. \quad (\text{C17})$$

As we have defined the necessary ingredients, we turn to defining the total energy density

$$w_{\text{tot}}^{\text{bub}} = \frac{E_{\text{tot}}^{\text{bub}}}{V_c}. \quad (\text{C18})$$

In our model, the total energy density includes 8 terms:

$$w_{\text{tot}}^{\text{bub}} = w_{\text{nuc}}^{\text{bub}} + w_{\text{p.surf}}^{\text{bub}} + w_{\text{C+L}}^{\text{bub}} + w_{\text{no}}^{\text{bub}} + w_{\text{e}}^{\text{bub}} + w_{\text{curv}}^{\text{bub}} + w_{\text{sk}}^{\text{bub}} + w_{\text{dc}}^{\text{bub}}. \quad (\text{C19})$$

The rest mass contribution due to baryons and the strong interaction contribution associated with the uniform matter inside the nucleus is given by

$$w_{\text{nuc}} = (1 - u^{\text{bub}})n [(1-x)m_n + xm_p]c^2 + (1 - u^{\text{bub}})n\varepsilon(n, x), \quad (\text{C20})$$

where ε is the energy per baryon specified in the Appendix.

The surface energy density $w_{\text{p.surf}}^{\text{bub}}$ is proportional to the surface area of the bubble and therefore has the form

$$w_{\text{p.surf}}^{\text{bub}} = \frac{u^{\text{bub}}d}{r_B} \sigma_s(x), \quad (\text{C21})$$

where $\sigma_s(x)$ is the function that has appeared in Eq. (B21). The Coulomb energy density including the nucleus self-energy and the lattice energy is [18, 49]

$$w_{\text{C+L}}^{\text{bub}} = 2\pi(enx r_B)^2 u^{\text{bub}} f_d(u^{\text{bub}}), \quad (\text{C22})$$

where the function $f_d(u)$ is given by Eq. (B23).

The energy density of the dripped neutrons $w_{\text{no}}^{\text{bub}}$ is

$$w_{\text{no}}^{\text{bub}} = u^{\text{bub}}n_{no} [m_n c^2 + \varepsilon(n_{no}, 0)], \quad (\text{C23})$$

the electron energy density w_{e} is

$$w_{\text{e}} = \frac{3}{4}\hbar c (3\pi^2)^{1/3} [(1 - u^{\text{bub}})nx]^{4/3}, \quad (\text{C24})$$

where we have used the electrical neutrality condition in the unit cell.

The energy density associated with curvature of the nucleus surface $w_{\text{curv}}^{\text{bub}}$ is proportional to both the surface area of the bubble and to the mean principal curvature of the surface of the nucleus, which is $2/r_B$ for 3D clusters, $1/r_B$ for 2D clusters and 0 for 1D clusters. Thus, it has the form

$$w_{\text{curv}}^{\text{bub}} = -\frac{u^{\text{bub}}d(d-1)}{r_B^2}\sigma_c. \quad (\text{C25})$$

Notice that the surface curvature contribution for bubbles has the opposite sign as compared with that for nuclei.

The energy density associated with the neutron skin can be written as

$$w_{\text{sk}}^{\text{bub}} = n_{\text{sk}}^{\text{bub}}\mu_{\text{sk}}, \quad (\text{C26})$$

where μ_{sk} is defined by the variational equation with respect to $n_{\text{sk}}^{\text{bub}}$.

Analogously, the energy density associated with the nuclear density curvature can be written as

$$w_{\text{dc}}^{\text{bub}} = n_{\text{dc}}^{\text{bub}}\mu_{\text{dc}}, \quad (\text{C27})$$

where μ_{dc} is defined by the variational equation with respect to $n_{\text{dc}}^{\text{bub}}$.

2. Variational equations

The variational equations have the form

$$\frac{\partial w_{\text{tot}}^{\text{bub}}}{\partial y} = 0, \quad (\text{C28})$$

where y is either of the variables from the set $\{n, x, n_{no}, r_B, u^{\text{bub}}, n_{\text{sk}}^{\text{bub}}, n_{\text{dc}}^{\text{bub}}\}$.

3. Optimum size of bubble

The derivative

$$\left. \frac{\partial (w_{\text{tot}}^{\text{bub}})}{\partial r_B} \right|_{n, x, n_{no}, u^{\text{bub}}, n_{\text{sk}}^{\text{bub}}, n_{\text{dc}}^{\text{bub}}} = 0 \quad (\text{C29})$$

leads to the nuclear virial theorem:

$$w_{\text{p.surf}}^{\text{bub}} + 2w_{\text{curv}}^{\text{bub}} = 2w_{\text{C+L}}^{\text{bub}}. \quad (\text{C30})$$

From Eq. (C30) we find the equation that determines r_N :

$$r_B^4 - 4q^{\text{bub}}r_B + 3r^{\text{bub}} = 0, \quad (\text{C31})$$

where

$$q^{\text{bub}} = \frac{1}{4} \frac{\sigma_s(x)d}{4\pi(enx)^2 f_d(u^{\text{bub}})}, \quad (\text{C32})$$

$$r^{\text{bub}} = \frac{1}{3} \frac{2d(d-1)\sigma_c(x)}{4\pi(enx)^2 f_d(u^{\text{bub}})}. \quad (\text{C33})$$

Notice a difference in signs in Eqs. (B33) and (C31). The solution to Eq. (C31) can be readily found using the methods of Ferrari and Cardano resulting in

$$r_B = \sqrt{\frac{p^{\text{bub}}}{2}} \left[1 + \sqrt{q^{\text{bub}} \left(\frac{2}{p^{\text{bub}}} \right)^{3/2} - 1} \right], \quad (\text{C34})$$

where

$$p^{\text{bub}} = \left[q^{\text{bub}2} + \sqrt{q^{\text{bub}4} - r^{\text{bub}3}} \right]^{1/3} + \left[q^{\text{bub}2} - \sqrt{q^{\text{bub}4} - r^{\text{bub}3}} \right]^{1/3}. \quad (\text{C35})$$

In case when the curvature contribution is neglected one obtains a simple result,

$$r_B = \left[\frac{\sigma_s(x)d}{4\pi(enx)^2 f_d(u^{\text{bub}})} \right]^{1/3}. \quad (\sigma_c = 0) \quad (\text{C36})$$

4. Chemical equilibrium

The derivative

$$\left. \frac{\partial (w_{\text{tot}}^{\text{bub}})}{\partial x} \right|_{n, n_{no}, r_B, u^{\text{bub}}, n_{\text{sk}}^{\text{bub}}, n_{\text{dc}}^{\text{bub}}} = 0 \quad (\text{C37})$$

provides the beta-equilibrium condition:

$$\mu_e^{\text{bub}} + (m_p - m_n)c^2 = - \left. \frac{\partial \epsilon}{\partial x} \right|_n - \frac{1}{(1 - u^{\text{bub}})n} \left. \frac{\partial (w_s^{\text{bub}} + w_{\text{curv}}^{\text{bub}} + w_{\text{C+L}}^{\text{bub}})}{\partial x} \right|_{n, n_{no}, r_B, u^{\text{bub}}}, \quad (\text{C38})$$

where

$$\mu_e^{\text{bub}} = \hbar c \left[3\pi^2(1 - u^{\text{bub}})xn \right]^{1/3}. \quad (\text{C39})$$

Again, the chemical equilibrium condition can be written as

$$\mu_e^{\text{bub}} = \mu_{ni}^{\text{bub}} - \mu_{pi}^{\text{bub}}, \quad (\text{C40})$$

where the neutron and the proton chemical potentials are given below by Eqs. (C47) and (C49), respectively.

5. Continuity of neutron chemical potential across the bubble interface

The derivative

$$\left. \frac{\partial (w_{\text{tot}}^{\text{bub}})}{\partial n_{ni}} \right|_{N_n, n_{pi}, r_B, u^{\text{bub}}, n_{\text{sk}}^{\text{bub}}, n_{\text{dc}}^{\text{bub}}} = 0 \quad (\text{C41})$$

implies that the energy to add a neutron to the nuclear matter outside the bubble is equal to the energy to add a neutron to the dripped neutrons inside the bubble, $\mu_{ni}^{\text{bub}} = \mu_{no}^{\text{bub}}$.

To obtain the explicit form of this condition we note that fixing of $N_n, n_{pi}, r_B, u^{\text{bub}}$ induces the following relations:

$$n\delta x + x\delta n = 0, \quad (\text{C42})$$

$$(1 - u^{\text{bub}})\delta n_{ni} + u^{\text{bub}}\delta n_{no} = 0. \quad (\text{C43})$$

The partial derivative is given by:

$$\begin{aligned} \frac{\partial}{\partial n_{ni}} \Big|_{N_n, n_{pi}, r_B, u^{\text{bub}}, n_{sk}^{\text{bub}}, n_{dc}^{\text{bub}}} &= \\ \frac{\partial}{\partial n} \Big|_{x, n_{no}, r_B, u^{\text{bub}}, n_{sk}^{\text{bub}}, n_{dc}^{\text{bub}}} + \frac{\delta x}{\delta n} \frac{\partial}{\partial x} \Big|_{n, n_{no}, r_B, u^{\text{bub}}, n_{sk}^{\text{bub}}, n_{dc}^{\text{bub}}} & \\ + \frac{\delta n_{no}}{\delta n_{ni}} \frac{\partial}{\partial n_{no}} \Big|_{n, x, r_B, u^{\text{bub}}, n_{sk}^{\text{bub}}, n_{dc}^{\text{bub}}} &. \end{aligned} \quad (\text{C44})$$

Using Eqs. (C42) and (C43), we find

$$\begin{aligned} \frac{\partial}{\partial n_{ni}} \Big|_{N_n, n_{pi}, r_B, u^{\text{bub}}, n_{sk}^{\text{bub}}, n_{dc}^{\text{bub}}} &= \\ \frac{\partial}{\partial n} \Big|_{x, n_{no}, r_B, u^{\text{bub}}, n_{sk}^{\text{bub}}, n_{dc}^{\text{bub}}} - \frac{x}{n} \frac{\partial}{\partial x} \Big|_{n, n_{no}, r_B, u^{\text{bub}}, n_{sk}^{\text{bub}}, n_{dc}^{\text{bub}}} & \\ - \frac{1 - u^{\text{bub}}}{u^{\text{bub}}} \frac{\partial}{\partial n_{no}} \Big|_{n, x, r_B, u^{\text{bub}}, n_{sk}^{\text{bub}}, n_{dc}^{\text{bub}}} &. \end{aligned} \quad (\text{C45})$$

Application of these partial derivatives yields

$$\mu_{ni}^{\text{bub}} = \mu_{no}^{\text{bub}}, \quad (\text{C46})$$

where

$$\begin{aligned} \mu_{ni}^{\text{bub}} &= m_n c^2 + \left(\frac{\partial}{\partial n} \Big|_x - \frac{x}{n} \frac{\partial}{\partial x} \Big|_n \right) [n\mathcal{E}(n, x)] \\ &- \frac{x}{(1 - u^{\text{bub}})n} \frac{\partial (w_{\text{p.surf}}^{\text{bub}} + w_{\text{cur}}^{\text{bub}})}{\partial x} \Big|_{r_B, u^{\text{bub}}}, \end{aligned} \quad (\text{C47})$$

and

$$\mu_{no}^{\text{bub}} = \frac{1}{u^{\text{bub}}} \frac{\partial w_{\text{no}}^{\text{bub}}}{\partial n_{no}} \Big|_{u^{\text{bub}}}. \quad (\text{C48})$$

By combining Eqs. (C38), (C40) and (C47) we find the proton chemical potential outside the bubble including the surface and Coulomb corrections:

$$\begin{aligned} \mu_{pi}^{\text{bub}} &= m_p c^2 + \left(\frac{\partial}{\partial n} \Big|_x + \frac{1 - x}{n} \frac{\partial}{\partial x} \Big|_n \right) [n\mathcal{E}(n, x)] \\ &+ \frac{1 - x}{(1 - u^{\text{bub}})n} \frac{\partial (w_{\text{p.surf}}^{\text{bub}} + w_{\text{cur}}^{\text{bub}})}{\partial x} \Big|_{r_B, u^{\text{bub}}, n_{sk}^{\text{bub}}, n_{dc}^{\text{bub}}} \\ &+ \frac{1}{(1 - u^{\text{bub}})n} \frac{\partial (w_{\text{C+L}}^{\text{bub}})}{\partial x} \Big|_{n, r_B, u^{\text{bub}}, n_{sk}^{\text{bub}}, n_{dc}^{\text{bub}}}. \end{aligned} \quad (\text{C49})$$

6. Continuity of pressure across the bubble interface

The derivative

$$\frac{\partial (w_{\text{tot}}^{\text{bub}})}{\partial u^{\text{bub}}} \Big|_{N_n, N_{no}, x, V_c, n_{sk}^{\text{bub}}, n_{dc}^{\text{bub}}} = 0 \quad (\text{C50})$$

implies that the energy density is minimized by choosing the optimal size of the nucleus while keeping fixed the cell size, the number of neutrons inside the nucleus, the number of neutrons outside the nucleus and the proton fraction. As a result, the pressure in the nucleus is equal to the pressure in the dripped neutrons, $P_i^{\text{bub}} = P_o^{\text{bub}}$.

Fixing N_n, N_{no}, x and V_c induces the following relations:

$$(1 - u^{\text{bub}})\delta n - n\delta u^{\text{bub}} = 0, \quad (\text{C51})$$

$$n_{no}\delta u^{\text{bub}} + u^{\text{bub}}\delta n_{no} = 0. \quad (\text{C52})$$

The partial derivative is given by:

$$\begin{aligned} \frac{\partial}{\partial n_{ni}} \Big|_{N_n, n_{pi}, r_B, u^{\text{bub}}} &= \frac{\partial}{\partial u^{\text{bub}}} \Big|_{n, x, n_{no}, V_c} \\ + \frac{\delta n}{\delta u^{\text{bub}}} \frac{\partial}{\partial n} \Big|_{n_{no}, x, r_B, u^{\text{bub}}} &+ \frac{\delta n_{no}}{\delta u^{\text{bub}}} \frac{\partial}{\partial n_{no}} \Big|_{n, x, r_B, u^{\text{bub}}}. \end{aligned} \quad (\text{C53})$$

Using Eqs. (C51) and (C52), we find

$$\begin{aligned} \frac{\partial}{\partial u^{\text{bub}}} \Big|_{N_n, N_{no}, x, V_c} &= \frac{\partial}{\partial u^{\text{bub}}} \Big|_{n, x, n_{no}, V_c} \\ + \frac{n}{1 - u^{\text{bub}}} \frac{\partial}{\partial n} \Big|_{n_{no}, x, r_B, u^{\text{bub}}} &- \frac{n_{no}}{u^{\text{bub}}} \frac{\partial}{\partial n_{no}} \Big|_{n, x, r_B, u^{\text{bub}}}. \end{aligned} \quad (\text{C54})$$

Making use of the relation

$$\partial [(1 - u^{\text{bub}})n] / \partial u^{\text{bub}} \Big|_{N_n, N_{no}, x, V_c} = 0, \quad (\text{C55})$$

we apply these partial derivatives and obtain

$$P_i^{\text{bub}} = P_o^{\text{bub}}, \quad (\text{C56})$$

where

$$\begin{aligned} P_i^{\text{bub}} &= n^2 \frac{\partial \mathcal{E}}{\partial n} \Big|_x \\ &+ \left(\frac{\partial}{\partial u^{\text{bub}}} \Big|_{n, x, n_{no}, V_c} + \frac{n}{1 - u^{\text{bub}}} \frac{\partial}{\partial n} \Big|_{n_{no}, r_B, u^{\text{bub}}} \right) \\ &\times (w_{\text{p.surf}}^{\text{bub}} + w_{\text{cur}}^{\text{bub}} + w_{\text{C+L}}^{\text{bub}}), \end{aligned} \quad (\text{C57})$$

and

$$\begin{aligned} P_o^{\text{bub}} &= \frac{n_{no}}{u^{\text{bub}}, n_{sk}^{\text{bub}}, n_{dc}^{\text{bub}}} \frac{\partial w_{\text{no}}^{\text{bub}}}{\partial n_{no}} \Big|_{u^{\text{bub}}} - \frac{w_{\text{no}}^{\text{bub}}}{u^{\text{bub}}} \\ &= n_{no}^2 \frac{\partial \mathcal{E}(n_{no}, 0)}{\partial n_{no}}. \end{aligned} \quad (\text{C58})$$

With the help of Eq. (B56) and the relations

$$\partial(u^{\text{bub}}/r_B)/\partial u^{\text{bub}}\Big|_{V_c} = (d-1)/r_B d, \quad (\text{C59})$$

$$\partial(u^{\text{bub}}/r_B^2)/\partial u^{\text{bub}}\Big|_{V_c} = (d-2)/r_B d, \quad (\text{C60})$$

$$\partial(r_B^2)/\partial u\Big|_{V_c} = 2r_B^2/u^{\text{bub}} d, \quad (\text{C61})$$

the derivatives within P_i^{bub} are calculated as following:

$$\frac{\partial w_{\text{p.surf}}^{\text{bub}}}{\partial u}\Big|_{N_n, N_{no}, x, V_c} = \frac{d-1}{r_B} \sigma_s(x), \quad (\text{C62})$$

$$\frac{\partial w_{\text{cur}}^{\text{bub}}}{\partial u}\Big|_{N_n, N_{no}, x, V_c} = -\frac{(d-2)(d-1)}{r_B^2} \sigma_c(x), \quad (\text{C63})$$

and

$$\begin{aligned} & \left(\frac{\partial}{\partial u}\Big|_{n, x, n_{no}, V_c} + \frac{n}{1-u^{\text{bub}}} \frac{\partial}{\partial n}\Big|_{n_{no}, r_B, u^{\text{bub}}} \right) w_{\text{C+L}}^{\text{bub}} \\ &= 2\pi(\text{exnr}_B)^2 \\ & \times \left[\left(\frac{2+d}{d} + \frac{2u^{\text{bub}}}{1-u^{\text{bub}}} \right) f_d(u^{\text{bub}}) + u^{\text{bub}} \partial_{u^{\text{bub}}} f_d(u^{\text{bub}}) \right]. \end{aligned} \quad (\text{C64})$$

7. Optimal energy to add neutron to the skin or to the density curvature region

Analogously to the case of nuclei, the conditions

$$\frac{\partial(E_{\text{tot}}^{\text{bub}}/V_c)}{\partial n_{\text{sk}}^{\text{bub}}}\Big|_{n, x, N_n, r_B, u^{\text{bub}}, n_{\text{dc}}^{\text{bub}}} = 0 \quad (\text{C65})$$

and

$$\frac{\partial(E_{\text{tot}}^{\text{bub}}/V_c)}{\partial n_{\text{dc}}^{\text{bub}}}\Big|_{n, x, N_n, r_B, u^{\text{bub}}, n_{\text{sk}}^{\text{bub}}} = 0 \quad (\text{C66})$$

simply lead to

$$\mu_{\text{sk}} = \mu_{\text{no}}^{\text{bub}}, \quad (\text{C67})$$

$$\mu_{\text{dc}} = \mu_{\text{no}}^{\text{bub}}. \quad (\text{C68})$$

Appendix D: Nuclear surface tension with curvature corrections

To obtain self-consistently the nuclear surface tension with curvature corrections, let us start considering a neutron-rich nucleus in equilibrium with a liquid of dripped neutrons. The problem of finding the density profile is formally similar to the one found in hot nucleus in equilibrium with the pure liquid phase. It is known that in this scenario the variational equations at given temperature and chemical potential possess two different solutions in both, quantum [50] and semiclassical descriptions [51]. One of these solutions represents the

nucleus-plus-liquid system and the another one to the pure liquid. Therefore, it seems natural to define the extensive quantities in the nucleus as the differences of their values in the nucleus-plus-liquid and the pure-liquid system.

To simplify this calculation, we simulate the nucleus as a half-space filled by uniform nuclear matter ($\tilde{z} < 0$), while the other half-space is filled by the pure neutron liquid ($\tilde{z} > 0$). As a consequence, in this geometry the energy per unit area, i.e. the surface tension, of nucleus constrained by the conservation of the neutron and protons numbers reads [34]:

$$\sigma_s = \int_{-\infty}^{+\infty} d\tilde{z} [\varepsilon(\tilde{z}) - \varepsilon_{no} - \mu_n(n_n(\tilde{z}) - n_{no}) - \mu_p n_p(\tilde{z})], \quad (\text{D1})$$

where ε_d is the energy density of the neutron liquid and $\varepsilon(\tilde{z})$ is the local energy density of the nucleus plus pure liquid (LG) system, which in the $\tilde{z} \rightarrow -\infty$ corresponds to the energy density ε_0 of uniform asymmetric nuclear matter in equilibrium with the uniform liquid of dripped neutrons (G). Here, $n_n(\tilde{z})$ is the total number density of neutrons at the plane $\tilde{z} = \text{const}$, n_{no} is the number density of neutrons of the pure neutron liquid at $\tilde{z} \rightarrow +\infty$ and $n_p = n_p(\tilde{z})$ is the number density of the proton component of nuclear matter.

The neutron and proton density profiles as well as the density of dripped neutrons are the solution of the Euler-Lagrange equations associated to Eq.(D1):

$$\frac{\delta \varepsilon(\tilde{z})}{\delta n_n} - \mu_n = 0, \quad \frac{\delta \varepsilon(\tilde{z})}{\delta n_p} - \mu_p = 0, \quad \frac{\delta \varepsilon_{no}}{\delta n_{no}} - \mu_n = 0, \quad (\text{D2})$$

where μ_n and μ_p are the neutron and proton chemical potentials computed at $\tilde{z} \rightarrow -\infty$, i.e. corresponding to the bulk phase in equilibrium with the dripped neutron liquid, which due to the equilibrium has the same neutron chemical potential, and $\varepsilon_{no} = \varepsilon(n = n_{no}, x = 0)$. The Euler-Lagrange equations (D2) is a set of coupled second order differential equations that are solved using the imaginary time-step method and provide the self-consistent neutron and proton densities in the LG and G phases. It is worthwhile to mention here that the surface tension defined by Eq. (D1) corresponds to the surface contribution to the thermodynamical potential $\Omega = E - \mu_n N - \mu_p Z = -PV$ in the LG phase, which is the quantity that has to be minimum in the thermodynamical equilibrium between the LG and G phases [35].

The surface tension in Eq. (D1) has been obtained under the assumption of a planar interface. In order to take into account that the interface is curved, we add an additional curvature correction that takes into account the curvature of the interface [35]. This corresponds to a Taylor expansion of the surface tension in the curved interface around the planar one. The lowest order corresponds to the planar surface tension, Eq. (D1). The correction term, which is linear in the principal curvature κ of the surface, is the curvature correction, which reads [34, 35]:

$$\sigma_c = \int_{-\infty}^{+\infty} d\tilde{z} [\varepsilon(\tilde{z}) - \varepsilon_{no} - \mu_n(n_n(\tilde{z}) - n_{no}) - \mu_p n_p(\tilde{z})](\tilde{z} - z_p), \quad (\text{D3})$$

where z_p is the proton surface location, which is defined as $\int_{-\infty}^{+\infty} d\tilde{z}(\tilde{z} - z_p)n'_p(\tilde{z}) = 0$. If we assume a constant proton density profile, this implies that all the protons are in the high

density phase, i.e. there are no dripped protons in accordance with the hypothesis of the LDM.

In Table III we display our data for the nuclear surface σ_s (in units of MeV fm^{-2}), the curvature σ_c (in units of MeV fm^{-1}) tensions and their derivatives with respect to x , which are needed to find the solution to the basic equations.

The data for the surface tension may be fitted by the analytical fits. For the planar surface tension, the fit is given in Eq. (9). For the curvature correction, the fit is

$$\sigma_c^{\text{fit}}(x) = \frac{\sigma_{c0}}{\sigma_0} \sigma_s^{\text{fit}}(x) \alpha_c (\beta_c - x). \quad (\text{D4})$$

For Sk χ 450, we find $\sigma_{c0} = 0.4612$, $\alpha_c = 3.9027$ and $\beta_c = 0.7562$.

We can also determine the neutron reference position of the neutron interface z_n in a similar way to that used to get z_p . Once the both interface positions, z_n and z_p , are known, we can define the neutron skin thickness as $s_n = z_n - z_p$. This surface layer contains mainly neutrons, which can be considered as adsorbed onto the proton surface located at z_p . The number of neutrons in this layer per unit surface is given by $N_s/S = (n_{n0} - n_{no})s_n$ [34, 35], where S is the surface area, n_{n0} is the neutron density in the bulk of nuclear matter.

There are additional contributions to the adsorbed neutrons due to the curvature of the proton surface, which per unit length L are given by $N_c/L = (n_{n0} - n_{no})(b_n^2 - b_p^2 + s_n^2)/2$ [34, 35], where b_n and b_p are the surface width of the neutron and proton densities defined as

$$b_n^2 = \frac{\int_{-\infty}^{+\infty} d\tilde{z} (\tilde{z} - z_n)^2 n'_n(\tilde{z})}{\int_{-\infty}^{+\infty} n'_n(\tilde{z})}, \quad b_p^2 = \frac{\int_{-\infty}^{+\infty} d\tilde{z} (\tilde{z} - z_p)^2 n'_p(\tilde{z})}{\int_{-\infty}^{+\infty} n'_p(\tilde{z})}. \quad (\text{D5})$$

Appendix E: Force acting on a single slab with neutron superflow in magnetic field

The basic assumption of the model developed in [3], is that the system is a toroidal volume containing ideal 1N phase. The slabs are oriented along the field lines of the toroidal component \mathbf{B} of the stellar magnetic induction, as schematically shown in Fig. 11 (a).

Let us now ‘‘cut’’ a piece of 1N phase in the inner crust, with spatial dimensions $D \times L^2$, as schematically shows thin rectangle in Fig. 11 (a). This rectangle is enlarged in Fig. 11 (b) in order to clearly define the physical system under consideration. By cutting a piece with $2r_N \ll L \ll R_*$, where R_* is the stellar radius, we convert the physical problem of the inner crust shown in Fig. 11 (a) into an idealized model where the slabs are strictly flat as shown in Fig. 11 (b). This situation corresponds to the model shown in Fig. 8 (a).

We assume periodic boundary conditions for the nucleon number currents in the plane parallel to the slab, so that the neutron and proton flows parallel to the slab surface are possible. If the condition $d_L > \xi$ is satisfied, the slabs in Fig. 8 (a) are independent, and therefore it is sufficient to consider only a single slab, as shown in Fig. 8 (c).

x	σ_s	$\partial\sigma_s/\partial x$	σ_c	$\partial\sigma_c/\partial x$
0.025	1.23×10^{-4}	0.01154	-1.0×10^{-4}	0.125813
0.0375	9.91×10^{-4}	0.130393	0.001521	0.187507
0.05	0.003427	0.259847	0.005366	0.436
0.0625	0.007467	0.38018	0.012058	0.552647
0.075	0.012954	0.505293	0.018796	0.550167
0.0875	0.02018	0.652033	0.026064	0.636813
0.1	0.029337	0.817933	0.034889	0.76712
0.1125	0.040726	1.007927	0.04528	0.89944
0.125	0.054632	1.22098	0.057456	1.05268
0.1375	0.071351	1.458293	0.071684	1.22674
0.15	0.09119	1.719793	0.088219	1.424907
0.1625	0.114446	2.0058	0.107373	1.637987
0.175	0.141423	2.313307	0.129232	1.86716
0.1875	0.172345	2.63714	0.15409	2.10664
0.2	0.207386	2.969667	0.181881	2.34342
0.2125	0.246579	3.300753	0.212569	2.554153
0.225	0.289845	3.617873	0.245551	2.717393
0.2375	0.336904	3.90494	0.280327	2.84238
0.25	0.387305	4.152653	0.316336	2.896993
0.2625	0.440518	4.351273	0.352492	2.888607
0.275	0.495859	4.494633	0.388322	2.826707
0.2875	0.552645	4.580827	0.422924	2.705407
0.3	0.610126	4.60614	0.455786	2.5453
0.3125	0.66753	4.567813	0.486393	2.3485
0.325	0.724018	4.462667	0.514279	2.11932
0.3375	0.778609	4.234893	0.538593	1.68658
0.35	0.829358	3.860047	0.555488	0.963347
0.3625	0.875016	3.470013	0.563078	0.369047
0.375	0.916267	3.131693	0.565657	0.046033
0.3875	0.953379	2.8083	0.564588	-0.207787
0.4	0.986508	2.49228	0.560663	-0.41674
0.4125	1.015699	2.17876	0.554294	-0.597733
0.425	1.040985	1.86714	0.545816	-0.755767
0.4375	1.062381	1.556307	0.535472	-0.896807
0.45	1.079893	1.245467	0.523452	-1.024547
0.4625	1.093517	0.934433	0.509903	-1.141693
0.475	1.103253	0.623213	0.494946	-1.250187
0.4875	1.109096	0.311627	0.478678	-1.351613
0.5	1.111043	-1.2×10^{-4}	0.46118	-1.4472

TABLE III. The leading (planar surface) contribution $\sigma_s(x)$ and the next-to-leading (principal curvature) correction $\sigma_c(x)$, for the surface tension of a thin surface, and their derivative with respect to the proton fraction x , as functions of x . The results obtained on the basis of a unified (self-consistent) description of the bulk and surface nuclear properties by the single Sk χ 450 interaction.

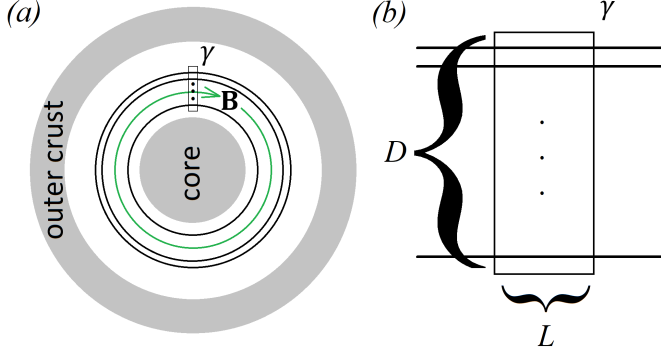


FIG. 11. (Color online). Panel (a): A schematic representation (not to the scale) of the magnetic-equatorial cross-section of the star, highlighting the 1N phase located between the outer crust (when mean baryon density n_b is smaller than the neutron drip density) and the core (when $n_b > n_0 \eta_{\text{uni}}^*$) and threaded by the toroidal lines of the stellar magnetic induction \mathbf{B} . Thin solid rectangle denoted as γ represents the cut piece of the toroidal volume shown in Fig. 8. Panel (b): Enlarged view of 2-dimensional projection of 3-dimensional piece of volume γ “cut” from panel (a), where D is the height of the column discussed in Eq. (33). The planar nature of the system seen in panel (b) and in Fig. 8 is due to the very large curvature radius of the structure as compared with the structure lattice period, while the periodic boundary conditions in the plane parallel to the slabs, which are used in our calculations are essential for existence of the neutron superflow. The parameter L was introduced in Eq. (B6).

Physically, a single slab in the magnetic field develops electric currents flowing inside the superconducting domain parallel to the surface and attempting to screen the magnetic field. Because of the form of the equilibrium vector potential \mathbf{A}_0 , the electric currents at the opposite surfaces of the slab have opposite directions. The electrons can be assumed static, because the opposite surfaces of the slab are separated by less than the screening length k_{TF}^{-1} shown in Fig. 9.

Following [3], we assume that the temperature is low enough, so that the superfluid nucleon densities are equal to the bulk nucleon densities n_α , ($\alpha = p, n$). The superconducting and superfluid S-wave order parameters $\sqrt{n_\alpha} \exp i\phi_\alpha$ consist of the superfluid density n_α and the superfluid phase ϕ_α . The fluid specific momenta are given by $\mathbf{p}_\alpha = \hbar \nabla \phi_\alpha$. The energy density of the system shown in Fig. 8 (c) is given by

$$w_{\text{tot}}^{\text{matt}} = w^{\text{nuc}} + w_{\text{kin}}^{\text{nuc}} + w_{\text{Coul}}^{\text{ep}} + w^e, \quad (\text{E1})$$

where w^{nuc} is given in Eq. (B20), w^e is given in Eq. (B25), $w_{\text{Coul}}^{\text{ep}} = e(n_p - n_e)\Phi$, Φ is the electrostatic potential, and the density of kinetic energy of the nucleons is

$$w_{\text{kin}}^{\text{nuc}} = \frac{n_p \pi_p^2}{2m} + \frac{n_n p_n^2}{2m} - \frac{n_{np}}{2m} (\pi_p - \mathbf{p}_n)^2. \quad (\text{E2})$$

Here, $\boldsymbol{\pi}_p = \mathbf{p}_p - e\mathbf{A}/c$ is the gauge-invariant proton momentum, \mathbf{A} is the electromagnetic vector potential, $\mathbf{w} = (\boldsymbol{\pi}_p -$

$\mathbf{p}_n)/m$ is the momentum lag, with $m = m_p \approx m_n$ and $\mathbf{B} = \nabla \times \mathbf{A}$.

The equations of motion generated from the energy functional with density given in Eq. (E1) have the form of the continuity equations and the Newton’s second law for each of the nucleon species [3]:

$$\partial_t n_\alpha + \nabla \cdot \mathbf{J}_\alpha = 0, \quad (\text{E3})$$

$$\partial_t \mathbf{p}_\alpha = -\nabla \frac{\partial w_{\text{tot}}^{\text{matt}}}{\partial n_\alpha}, \quad (\text{E4})$$

where \mathbf{J}_α are the number currents of each species of nucleons. Combining the momentum equations we arrive at the expression for the total force acting under the given conditions.

Using the geometry shown in Fig. 8 (c), the equilibrium vector potential is $\mathbf{A}_0 = -\hat{\mathbf{y}} B_0 z$ and the unperturbed superfluid gauge-invariant momentum lag \mathbf{w}_0 is given by

$$\mathbf{w}_0 = (e/mc)\hat{\mathbf{y}} B_0 z, \quad (\text{E5})$$

see equation (35) in [3]. The force is zero in equilibrium, as also can be seen from Eq. (28) with $\mathbf{w} = \mathbf{w}_0$.

Let us study perturbation of the force as a result of perturbation of the neutron superflow. Notice that there is no back action of this force upon the source of the field \mathbf{H} , because this force is merely an extra fluid pressure gradient, which upon integration of the total force in the entire volume of the superconducting body, gives zero, as expected from the total momentum conservation. The integration gives zero because of the axial symmetry of the system as reveals Fig. 11 (a). In the coordinates shown in Fig. 8 (c), the relevant force with $L = 1$ cm is given by

$$\delta^{(1)} \mathbf{F}_{\text{tot}}^{1 \text{ cm}^2 \times 2r_c} = \hat{\mathbf{z}} \int d^3 \mathbf{r} \sum_k \nabla_k \Pi_{3k}, \quad (\text{E6})$$

where the stress tensor is

$$\Pi_{ik} = J_{pk} \pi_{pi} + J_{nk} p_{ni} + \delta_{ik} P + \frac{1}{4\pi} (\delta_{ik} \frac{B^2}{2} - B_k B_i). \quad (\text{E7})$$

Here, $\rho_{np}^* = mn_{np} - mn_p \theta_p - mn_n \theta_n$ is the entrainment mass density (in the Skyrme model, $\theta_p = \theta_n = 0$), n_{np} is the entrainment number density and P is the total physical pressure (the hydrodynamic pressure). We evaluate the entrainment number density from (see Eq. (49) in [43])

$$n_{np} = \frac{2}{n_0} \left(1 - \frac{m}{m_0^*} \right) n_n n_p, \quad (\text{E8})$$

where n_p and n_n are the nucleon number densities in uniform matter, m_0^* is the nucleon so-called *isovector* effective mass, which is given by (see Eq. (3.22) in [38])

$$\frac{m}{m_0^*} = 1 + \frac{m}{4\hbar^2} n_0 [t_1 (x_1 + 2) + t_2 (x_2 + 2)]. \quad (\text{E9})$$

The isovector effective mass is related to the effective mass given in Eq. (A2) as following:

$$m_0^* = \tilde{m}_q|_{n_q=0}. \quad (\text{E10})$$

P is generally defined as the material contribution to Π_{ik} associated with the isotropic tensor δ_{ik} . The hydrodynamic pressure is given by [3]

$$P = p - \rho_{np}^* \mathbf{w}^2 / 2, \quad (\text{E11})$$

where p is the pressure without the contributions due to the matter flows as given by equation (32) in [3]. The hydrostatic pressure p is irrelevant in order to calculate the additional pressure due to the peculiar force and thus it is taken constant across the slab. The crustal stress appears in the problem as soon as we impose condition that the slab is static due to external forces at the boundary γ of the domain, see Fig. 11. In this case p becomes spatially dependent to compensate the

additional pressure, and this affects the resulting total momentum flux at the domain boundary thus loading the crust until the resulting strain reaches a critical value.

It remains to evaluate the total force as a resultant of the forces applied to each of the slabs in the lattice (see Fig. 8 (a)). From independence of the slabs, the total force acting on a $1 \text{ cm}^2 \times D$ column of lasagna is a sum of (integer part of) $D/2r_c$ equal terms, or

$$\delta \mathbf{F}_{\text{tot}}^{1 \text{ cm}^2 \times D} = \frac{D}{2r_c} \delta^{(1)} \mathbf{F}_{\text{tot}}^{1 \text{ cm}^2 \times 2r_c}, \quad (\text{E12})$$

where D is the height of the column measured along the normal direction of the slabs.

-
- [1] M. E. Caplan and C. J. Horowitz, *Rev. Mod. Phys.* **89**, 041002 (2017). Colloquium: Astromaterial science and nuclear pasta. <https://doi.org/10.1103/RevModPhys.89.041002>
- [2] G. Baym, C. Pethick and D. Pines, *Nature (London)*, **224**, 673 (1969). Superfluidity in Neutron Stars. <https://doi.org/10.1038/224673a0>
- [3] D. N. Kobyakov, *Phys. Rev. C* **98**, 045803 (2018). Application of Superconducting-Superfluid Magneto-hydrodynamics to Nuclear “Pasta” in Neutron Stars. <https://doi.org/10.1103/physrevc.98.045803>
- [4] D. N. Kobyakov and C. J. Pethick, *Sov. Phys. JETP* **127**, 851 (2018). Superfluid Liquid Crystals: Pasta Phases in Neutron Star Crusts. <https://doi.org/10.1134/s1063776118110067>
- [5] Z.-W. Zhang and C. J. Pethick, *Phys. Rev. C* **103**, 055807 (2021). Proton Superconductivity in Pasta Phases in Neutron Star Crusts. <https://doi.org/10.1103/physrevc.103.055807>
- [6] Y. Lim and J. W. Holt, *Phys. Rev. C* **103**, 025807 (2021). Proton Pairing in Neutron Stars from Chiral Effective Field Theory. <https://doi.org/10.1103/physrevc.103.025807>
- [7] R. A. Klemm, A. Luther and M. R. Beasley, *Phys. Rev. B* **12**, 877 (1975). Theory of the Upper Critical Field in Layered Superconductors. <https://doi.org/10.1103/PhysRevB.12.877>
- [8] G. Deutscher and O. Entin-Wohlman, *Phys. Rev. B* **17**, 1249 (1978). Critical Fields of Weakly Coupled Superconductors. <https://doi.org/10.1103/PhysRevB.17.1249>
- [9] L. Wang, H. S. Lim and C. K. Ong, *Supercond. Sci. Technol.* **14**, 252 (2001). Continuous Ginzburg-Landau Description of Layered Superconductors. <https://doi.org/10.1088/0953-2048/14/5/305>
- [10] D. Kobyakov and C. J. Pethick, *MNRAS Lett.* **449**, L110—L112 (2015). Elastic Properties of Polycrystalline Dense Matter. <https://doi.org/10.1093/mnrasl/slv027>
- [11] C. J. Pethick, Zhao-Wen Zhang and D. N. Kobyakov, *Phys. Rev. C* **101**, 055802 (2020). Elastic Properties of Phases with Nonspherical Nuclei in Dense Matter. <https://doi.org/10.1103/PhysRevC.101.055802>
- [12] Z.-W. Zhang and C. J. Pethick, *Phys. Rev. C* **105**, 055807 (2022). Superfluid Density in Disordered Pasta Phases in Neutron Star Crusts. <https://doi.org/10.1103/physrevc.105.055807>
- [13] W. G. Newton, S. Cantu, S. Wang, A. Stinson, M. A. Kaltenborn and J. R. Stone, *Phys. Rev. C* **105**, 025806 (2022). Glassy Quantum Nuclear Pasta in Neutron Star Crusts. <https://doi.org/10.1103/PhysRevC.105.025806>
- [14] J. W. Negele and D. Vautherin, *Nucl. Phys. A* **207**, 298 (1973). Neutron Star Matter at Sub-Nuclear Densities. [https://doi.org/10.1016/0375-9474\(73\)90349-7](https://doi.org/10.1016/0375-9474(73)90349-7)
- [15] C. Mondal, X. Viñas, M. Centelles and J.N. De, *Phys. Rev. C* **102**, 015802 (2020). Structure and Composition of the Inner Crust of Neutron Stars from Gogny Interactions. <https://doi.org/10.1103/PhysRevC.102.015802>
- [16] B. K. Sharma, M. Centelles, X. Viñas, M. Baaldo and F. Burgio, *Astron. Astrophys.* **584**, A103 (2015). Unified Equation of State for Neutron Stars on a Microscopic Basis. <https://doi.org/10.1051/0004-6361/201526642>
- [17] G. Baym, H. A. Bethe and C. J. Pethick, *Nuclear Physics A* **175**, 225 (1971). Neutron Star Matter. [https://doi.org/10.1016/0375-9474\(71\)90281-8](https://doi.org/10.1016/0375-9474(71)90281-8)
- [18] D. G. Ravenhall, C. J. Pethick and J. R. Wilson, *Phys. Rev. Lett.* **50**, 2066 (1983). Structure of Matter below Nuclear Saturation Density. <https://doi.org/10.1103/PhysRevLett.50.2066>
- [19] M. Hashimoto, H. Seki and M. Yamada, *Progr. Theor. Phys.* **71**, 320 (1984). Shape of Nuclei in the Crust of Neutron Star. <https://doi.org/10.1143/PTP.71.320>
- [20] W.D. Myers and W.J. Swiatecki, *Ann. Phys.* **55**, 395 (1969). Average nuclear properties. [https://doi.org/10.1016/0003-4916\(69\)90202-4](https://doi.org/10.1016/0003-4916(69)90202-4)
- [21] W.D. Myers and W.J. Swiatecki, *Ann. Phys.* **84**, 186 (1974). The nuclear droplet model for arbitrary shapes. [https://doi.org/10.1016/0003-4916\(74\)90299-1](https://doi.org/10.1016/0003-4916(74)90299-1)
- [22] Y. Lim and J. W. Holt, *Phys. Rev. C* **95**, 065805 (2017). Structure of Neutron Star Crusts from New Skyrme Effective Interactions Constrained by Chiral Effective Field Theory. <https://doi.org/10.1103/PhysRevC.95.065805>
- [23] W. G. Newton, M. Gearheart and Bao-An Li, *Astrophys. J. Supp. Ser.* **204**, 9 (2013). A Survey of the Parameter Space of the Compressible Liquid Drop Model as Applied to the Neutron Star Inner Crust. <https://doi.org/10.1088/0067-0049/204/1/9>
- [24] T. Carreau, F. Gulminelli, N. Chamel, A.F. Fantina and J.M. Pearson, *Astron. Astrophys.* **635**, A84 (2020). Crystallization of the Inner Crust of a Neutron Star and the Influence of Shell Effects. <https://doi.org/10.1051/0004-6361/201937236>
- [25] T. Carreau, A.F. Fantina and F. Gulminelli, *Astron. Astrophys.* **640**, A77 (2020). Inner Crust of a Neutron Star at the Point of Crystallization in a Multicomponent Approach. <https://doi.org/10.1051/0004-6361/202038347>
- [26] H. Dinh Thi, A. F. Fantina and F. Gulmonelli, *Eur. Phys. J. A* **57**, 296 (2021). The Effect of the Energy Functional on the Pasta-Phase Properties of Catalysed Neutron Stars.

- <https://doi.org/10.1140/epja/s10050-021-00605-6>
- [27] H. Dinh Thi, T. Carreau, A. F. Fantina and F. Gulminelli, *Astron. Astrophys.* **654**, A77 (2020). Uncertainties in the Pasta-Phase Properties of Catalysed Neutron Stars. <https://doi.org/10.1051/0004-6361/202141192>
- [28] L. E. Balliet, W. G. Newton, S. Cantu and S. Budimir, *Astrophys. J.* **918**, 79 (2021). Prior Probability Distributions of Neutron Star Crust Models. <https://doi.org/10.3847/1538-4357/ac06a4>
- [29] N. N. Shechchilin, N. A. Zemlyakov, A. I. Chugunov and M.E. Gusakov, *Symmetry* **8**, 582 (2022). Pasta Phases in Neutron Star Mantle: Extended Thomas–Fermi vs. Compressible Liquid Drop Approaches. <https://doi.org/10.3390/universe8110582>
- [30] D. G. Ravenhall, C. J. Pethick, J. M. Lattimer, *Nucl. Phys. A*, **407**, 571 (1983). Nuclear Interface Energy at Finite Temperatures. [https://doi.org/10.1016/0375-9474\(83\)90667-X](https://doi.org/10.1016/0375-9474(83)90667-X)
- [31] J. M. Lattimer C. J. Pethick, D. G. Ravenhall and D.Q. Lamb, *Nucl. Phys. A*, **432**, 646 (1985). Physical Properties of Hot, Dense Matter: The General Case. [https://doi.org/10.1016/0375-9474\(85\)90006-5](https://doi.org/10.1016/0375-9474(85)90006-5)
- [32] C. P. Lorentz, D. G. Ravenhall and C. J. Pethick, *Phys. Rev. Lett.* **70**, 379 (1993). Neutron Star Crusts. <https://doi.org/10.1103/PhysRevLett.70.379>
- [33] M. Brack, C. Guet and H.-B. Håkanson, *Phys. Rep.* **123**, 275 (1985). Selfconsistent Semiclassical Description of Average Nuclear Properties - a Link Between Microscopic and Macroscopic Models. [https://doi.org/10.1016/0370-1573\(86\)90078-5](https://doi.org/10.1016/0370-1573(86)90078-5)
- [34] M. Centeles, M. Del Estal and M. Vinas, *Nucl. Phys. A* **635**, 193 (1998). Semiclassical Treatment of Asymmetric Semi-infinite Nuclear Matter: Surface and Curvature Properties in Relativistic and Non-relativistic Models. [https://doi.org/10.1016/S0375-9474\(98\)00167-5](https://doi.org/10.1016/S0375-9474(98)00167-5)
- [35] F. Douchin, P. Haensel and J. Meyer, *Nucl. Phys. A*, **665**, 419 (2000). Nuclear Surface and Curvature Properties for SLy Skyrme Forces and Nuclei in the Inner Neutron-Star Crust. [https://doi.org/10.1016/S0375-9474\(99\)00397-8](https://doi.org/10.1016/S0375-9474(99)00397-8)
- [36] C. J. Pethick, D. G. Ravenhall, and C. P. Lorenz, *Nucl. Phys. A* **584**, 675 (1995). The inner boundary of a neutron star crust. [https://doi.org/10.1016/0375-9474\(94\)00506-I](https://doi.org/10.1016/0375-9474(94)00506-I)
- [37] J. Keller, K. Hebeler, C. J. Pethick, and A. Schwenk, *Phys. Rev. Lett.* **132**, 232701 (2024). Neutron Star Matter as a Dilute Solution of Protons in Neutrons. <https://doi.org/10.1103/PhysRevLett.132.232701>
- [38] E. Chabanat, P. Bonche, P. Haensel, J. Meyer, R. Schaeffer, *Nucl. Phys. A* **627**, 710 (1997). A Skyrme parametrization from subnuclear to neutron star densities. [https://doi.org/10.1016/S0375-9474\(97\)00596-4](https://doi.org/10.1016/S0375-9474(97)00596-4)
- [39] D. N. Kobyakov, *Phys. Rev. C* **102**, 045803 (2020). Surface Energy of Magnetized Superconducting Matter in Neutron Star Cores. <https://doi.org/10.1103/PhysRevC.102.045803>
- [40] Ian Easson and C. J. Pethick, *Phys. Rev. D* **16**, 275 (1977). Stress Tensor of Cosmic and Laboratory Type-II Superconductors. <https://doi.org/10.1103/PhysRevD.16.275>
- [41] A. D. Sedrakian and D. M. Sedrakian, *Astrophys. J.* **447**, 305 (1995). Superfluid Core Rotation in Pulsars. I. Vortex Cluster Dynamics. <https://doi.org/10.1086/175876>
- [42] D. N. Kobyakov, *Phys. Rev. C* **108**, 049901 (2023). Erratum: Application of superconducting-superfluid magnetohydrodynamics to nuclear “pasta” in neutron stars [*Phys. Rev. C* **98**, 045803 (2018)]. <https://doi.org/10.1103/PhysRevC.108.049901>
- [43] D. N. Kobyakov, C. J. Pethick, S. Reddy, A. Schwenk, *Phys. Rev. C* **96**, 025805 (2017). Dispersion and Decay of Collective Modes in Neutron Star Cores. <https://doi.org/10.1103/physrevc.96.025805>
- [44] M. Dutra, O. Lourenco, J. S. Sa Martins, A. Delfino, J. R. Stone and P. D. Stevenson, *Phys. Rev. C* **85**, 035201 (2012). Skyrme Interaction and Nuclear Matter Constraints. <https://doi.org/10.1103/PhysRevC.85.035201>
- [45] C. Gonzalez-Boquera, Ph.D. thesis, Universitat de Barcelona, September 2019; arXiv:2003.00490. Neutron-rich Matter in Atomic Nuclei and Neutron Stars. <https://doi.org/10.48550/arXiv.2003.00490>
- [46] G. Grams, R. Somasundaram, J. Margueron and S. Reddy, *Phys. Rev. C* **105**, 035806 (2022). Properties of the Neutron Star Crust: Quantifying and Correlating Uncertainties with Improved Nuclear Physics. <https://doi.org/10.1103/PhysRevC.105.035806>
- [47] G. Grams, J. Margueron, R. Somasundaram and S. Reddy, *Eur. Phys. J. A* **58**, 56 (2022). Confronting a Set of Skyrme and χ_{EFT} Predictions for the Crust of Neutron Stars. <https://doi.org/10.1140/epja/s10050-022-00706-w>
- [48] X. Vinas, M. Centelles, X. Roca-Maza, and M. Warda, *Eur. Phys. J. A* **50**, 27 (2014). Density Dependence of the Symmetry Energy from Neutron Skin Thickness in Finite Nuclei. <https://doi.org/10.1140/epja/i2014-14027-8>
- [49] C. J. Pethick and D. G. Ravenhall, *Annu. Rev. Nucl. Part. Sci.* **45**, 429 (1995). Matter at Large Neutron Excess and the Physics of Neutron-Star Crusts. <https://doi.org/10.1146/annurev.ns.45.120195.002241>
- [50] P. Bonche, S. Levit and D. Vautherin, *Nucl. Phys. A*, **436**, 265 (1985). Statistical Properties and Stability of Hot Nuclei. [https://doi.org/10.1016/0375-9474\(85\)90199-X](https://doi.org/10.1016/0375-9474(85)90199-X)
- [51] E. Suraud, *Nucl. Phys. A* **462**, 109 (1987). Semi-Classical Calculations of Hot Nuclei. [https://doi.org/10.1016/0375-9474\(87\)90382-4](https://doi.org/10.1016/0375-9474(87)90382-4)
- [52] C. A. van Eysden and A. Melatos, *MNRAS* **409**, 1253 (2010). Pulsar glitch recovery and the superfluidity coefficients of bulk nuclear matter. <https://doi.org/10.1111/j.1365-2966.2010.17387.x>